

## AN INSTRUMENT FOR INVESTIGATING THE LARGE ANGULAR SCALE POLARIZATION OF THE COSMIC MICROWAVE BACKGROUND

BRIAN G. KEATING<sup>1</sup>, CHRISTOPHER W. O'DELL, JOSHUA O. GUNDERSEN<sup>2</sup>, LUCIO PICCIRILLO<sup>3</sup>,  
NATE C. STEBOR<sup>4</sup>, AND PETER T. TIMBIE  
Department of Physics, 2531 Sterling Hall, University of Wisconsin – Madison, Madison, WI 53706  
*Draft version December 11, 2001*

### ABSTRACT

We describe the design and performance of a microwave polarimeter used to make precision measurements of polarized astrophysical radiation in three microwave frequency bands spanning 26-36 GHz. The instrument uses cooled HEMT amplifiers in a correlation polarimeter configuration to achieve high sensitivity and long-term stability. The instrument demonstrates long term stability and has produced the most restrictive upper limits to date on the large angular scale polarization of the 2.7 K cosmic microwave background radiation.

*Subject headings:* cosmic microwave background: – cosmology: observations, instrumentation, polarimeters

### 1. INTRODUCTION

Observations of the cosmic microwave background (CMB) have become some of the most powerful tools in cosmology. All modern cosmological theories must address the existence of the CMB, and observations of the the CMB have produced some of the most precise measurements in cosmology. Since the CMB is a probe of the primordial universe it has the promise to address the most fundamental cosmological questions: the geometry and age of the universe, the matter content of the universe, the ionization history, and the spectrum of primordial perturbations. The CMB is specified by three characteristics: its spectrum, spatial distribution of its total intensity, and the spatial distribution of its polarization. All three properties depend on the fundamental cosmological parameters. Several instruments have produced precision measurements of its spectrum and anisotropy at large, medium, and small angular scales (see, for example, Wang, Tegmark, & Zaldarriaga (2001) and references therein).

Similar to the CMB anisotropy power spectrum, the polarization power spectrum encodes information on all angular scales. Large angular scales ( $> 1^\circ$ ) correspond to regions on the last scattering surface which were larger than the causal horizon at that time. In the absence of reionization, polarization on these scales was affected only by the longest wavelength modes of the primordial power spectrum. Reionization is expected to produce a new polarized peak in the power spectrum near  $\ell \lesssim 20$ , where the precise peak location depends on the redshift at which the Universe (Zaldarriaga 1998; Keating et al. 1998) became reionized.

The large scale region of the anisotropy power spectrum was measured by the *COBE* DMR, and this established the normalization for models of large scale structure for-

mation. The effect of reionization on the anisotropy power spectrum is to damp all angular scales by a factor of  $e^{-2\tau}$  where  $\tau$  is the optical depth to the reionization epoch. This effect is degenerate with several other cosmological parameters (Zaldarriaga 1997) and non-zero  $\tau$  cannot be unambiguously detected, at any scale, from the anisotropy power spectrum alone. Similarly, the effect of gravitational waves on the anisotropy power spectrum is also degenerate with other cosmological parameters (Zaldarriaga, Spergel, & Seljak 1997). Detection of CMB polarization at scales  $> 1^\circ$  has the promise to produce robust measurements of reionization and primordial gravitational waves.

Since the anticipated polarization is small at all angular scales, polarization measurements pose a significant challenge. Although the polarization signal at large angular scales is expected to be weaker than at small scales, the design of a large angular scale experiment is simpler and more compact than an experiment probing small scales. A large angular scale experiment with no external beam forming optics (*i.e.*, no primary mirror), exhibits minimal spurious polarization and dramatically reduces susceptibility to systematic errors. In this paper we describe our approach to measuring the large scale polarization of the CMB: Polarization Observations of Large Angular Regions (POLAR).

POLAR's design builds on techniques developed in previous searches for CMB polarization (Nanos 1979; Lubin & Smoot 1981; Wollack et al. 1997) and is driven by the size and angular scale of the anticipated CMB signals, spectral removal of foreground sources, optimization of the observing scheme, long-term stability, and immunity to potential systematic effects. POLAR is a wide bandwidth ( $\sim 8$  GHz) correlation polarimeter dedicated to measurements of the CMB. POLAR measures polarization scales in the  $K_a$  band, between 26 and 36 GHz, using cooled High Electron Mobility Transistor amplifiers. This band is multiplexed into three sub-bands to allow for discrimination against foreground sources. The radiometer executes a zenith drift scan with a  $7^\circ$  FWHM beam produced by a corrugated feed horn antenna. In the Spring of 2000 POLAR observed a  $\simeq 7^\circ$  wide region from  $RA = 112^\circ$  to  $275^\circ$  at declination  $43^\circ$  for 45 days from the University of Wisconsin – Madison's Pine Bluff Observatory in Pine Bluff, Wisconsin

<sup>1</sup> Current Address: Division of Physics, Math, and Astronomy, California Institute of Technology, Pasadena, CA 91125; bgk@astro.caltech.edu.

<sup>2</sup> Department of Physics, University of Miami, Coral Gables, FL 33146

<sup>3</sup> Department of Physics and Astronomy, University of Wales - Cardiff, Wales, UK CF24 3YB

<sup>4</sup> Department of Physics, University of California at Santa Barbara, Santa Barbara, CA 93106

(Latitude  $+43^{\circ}01'$ , Longitude  $+89^{\circ}45'$ ). In a single night of data POLAR achieved a sensitivity level of  $\sim 50 \mu\text{K}$  to the Stokes parameters  $Q$  and  $U$  in each beam-sized pixel. For the 2000 season POLAR set upper limits on the amplitude of the cosmological E-mode and B-mode (Zaldarriaga & Seljak 1997; Kamionkowski, Kosowsky, & Stebbins 1997) power spectra of  $T_E, T_B < 10 \mu\text{K}$  at 95% confidence (Keating et al. 2001).

In this paper we describe the design and performance of POLAR. In section 2 we outline the fundamentals of the correlation polarimeter. Section 3 presents detailed instrument design specifications and performance. Section 4 describes our calibration technique, and section 5 addresses potential systematic effects and radiometric offset characterization. Finally, section 6 summarizes the meteorological conditions observed during the observation run as well as our data selection criteria.

## 2. CORRELATION POLARIMETER

The correlation polarimeter is based on a correlation radiometer (Fujimoto 1964; Rohlfs 1996). The development of the correlation radiometer preceded the discovery of the CMB in 1965; see for example Fujimoto (1964). Several early CMB experiments used correlation radiometers for anisotropy measurements (Cheng et al. 1979), spectral measurements (Johnson & Wilkinson 1987), and the first application of a dedicated interferometer to CMB research (Timbie & Wilkinson 1990). The correlation radiometer accomplishes Dicke switching by viewing a source with two different receivers, and subsequently correlating the out-

TABLE 1  
POLAR INSTRUMENT SPECIFICATIONS.

Channel <sup>a</sup>	$\nu_c^b$ [GHz]	$\Delta\nu^c$ [GHz]	$\Omega_B^d$ [ $^{\circ}$ ]	$\overline{T}_{\text{pol}}^e$ [ $\mu\text{K}$ ]	$S_{\text{sky}}^f$ [ $\text{mK s}^{1/2}$ ]	$T_{\text{rec}}^g$ [K]
TP-E/H	31.9	7.8/8.0	7.0	...	14.0/20.0	32
J3	27.5	1.3	7.5	84(28)	2.0	43
J2	30.5	3.1	7.0	72(14)	1.2	34
J1	34.0	3.1	6.4	33(11)	1.1	33

<sup>a</sup>TP-E and TP-H measure the total power in the E and H polarization planes of the Horn/OMT assembly prior to correlation.

<sup>b</sup>Channel Band Centroid

<sup>c</sup>Channel Bandwidth.

<sup>d</sup>Beamwidths (FWHM). E and H-plane Beamwidths are equal to within 1%. Measured feed/OMT cross-polarization is  $< -40\text{dB}$  for all channels.

<sup>e</sup>Mean Polarized Offset for the Spring 2000 observing season.  $\overline{T}_{\text{pol}} = \sqrt{\overline{Q}^2 + \overline{U}^2}$  where  $\overline{Q}$  and  $\overline{U}$  are the average Stokes parameter offsets for the season. Numbers in parentheses denote the corresponding values for the QPC.

<sup>f</sup>Measured channel NET for a typical clear day with  $K_a$ -band zenith sky temperature  $T_{\text{Atm}} \simeq 12\text{K}$ . NET measured at Stokes modulation frequency 0.065 Hz.

<sup>g</sup>Measured receiver temperature for each channel.

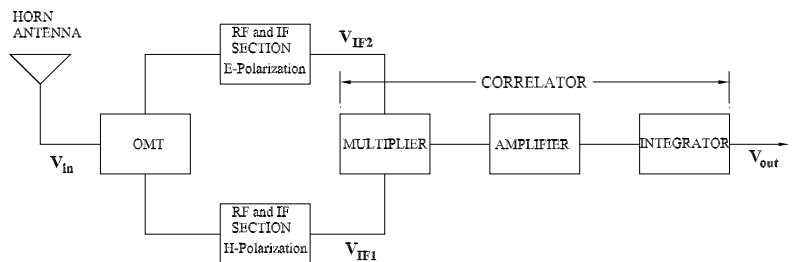


FIG. 1.— Schematic of a simple correlation polarimeter. Radio-frequency fields are split into two linear polarization states by an orthomode transducer (OMT), and amplified. The field amplitudes are multiplied, producing a DC voltage proportional to their product. The DC product voltage is filtered and amplified before being integrated (low-pass filtered) prior to being recorded.

puts at RF frequencies using a multiplier. The system has a  $\sqrt{2}$  noise advantage over the single receiver Dicke switched total power radiometer (Rohlfs 1996). The primary complications are the cost of the second receiver and the need to match the phase and gain of the two receivers over the across the RF bands. In a correlation polarimeter the two linear polarization components are amplified in separate parallel amplifier chains and the output signals are correlated, resulting in a signal proportional to the  $U$  Stokes parameter. Physically, the correlator (multiplier) is based on a non-linear device, such as a diode which acts as a mixer when provided with an AC bias waveform. The bias power for the diode comes from the uncorrelated RF power in each arm, which being in the RF band, effectively switches at these high radio frequencies. An advantage of this differencing mechanism is that it requires no moving parts which potentially can complicate CMB experiments of this type. A variation of this receiver design correlates left and right circular polarization modes, and is able to recover all four Stokes parameters simultaneously<sup>5</sup> (Sironi et al. 1997; Carretti et al. 2001). A simplified correlation polarimeter is shown in figure 1. Radiation from the sky couples into a feed horn which propagates both linear polarization modes. The orthomode transducer (OMT) separates the two polarization modes, sending each to a separate receiver. The multiplier forms the product of the two fields which is subsequently integrated. This multiplication and integration is equivalent to the statistical definition of the cross-correlation of the two polarization states, and is proportional to the Stokes  $U$  parameter. For a single frequency, the fields entering the multiplier are:

<sup>5</sup>A disadvantage of the circular mode correlation polarimeter is that conversion between  $Q$  and  $U$  can occur, whereas for linear correlation polarimeters (such as POLAR) primarily conversion between  $U$  and  $V$  (or  $Q$  and  $V$ ) occurs (Thompson et al. 1998; Carretti et al. 2001). Since  $V \ll Q, U$  (either cosmological or systematic), polarization conversion is negligible for POLAR. However, both correlation polarimeter methods suffer from conversion between  $I$  and  $Q$  and  $U$  as discussed below.

$$\begin{aligned} E_y(t) &= E_{y_o} \cos[\nu t + \phi_y(t)] + n_y(t) \\ E_x(t) &= E_{x_o} \cos[\nu t + \phi_x(t)] + n_x(t), \end{aligned}$$

where  $n_i$  is the noise waveform generated by the amplifier measuring polarization state  $i$  and  $\langle n_i(t)n_j(t) \rangle = \sigma^2 \delta_{ij}$ , where  $i \in \{E, H\}$ ,  $\sigma^2$  is the variance of the noise,  $n_i$ , (assumed to be the same for each amplifier) and the  $x, y$  basis is defined by the  $E$  and  $H$  planes of the OMT. The electric field magnitude at the OMT output at time  $t$  from a source in direction  $\theta$  (with respect to the feed boresight) is expanded into:

$$\begin{aligned} \tilde{E}_i(\theta, \nu) &= \int_{-\infty}^{+\infty} E(\theta, t) e^{-i2\pi\nu t} dt \\ E_i(\theta, t) &= \int_{-\infty}^{+\infty} \tilde{E}_i(\theta, \nu) e^{i2\pi\nu t} d\nu. \end{aligned}$$

The horn's voltage response function  $\tilde{G}(\theta, \nu)$  has dimension [length] (and is not equal to the power response function,  $\tilde{B}(\theta, \nu)$ , defined below) and is assumed to be axisymmetric. The antenna output voltage for polarization state  $i \in \{E, H\}$  is

$$\tilde{V}_i(\nu) = 2\pi \int_{-\pi}^{+\pi} \tilde{E}_i(\theta, \nu) \tilde{G}(\theta, \nu) d\theta. \quad (1)$$

The output voltage for each polarization, after amplification by the HEMT/mixer/IF amplifier chain, with total radiometer voltage transfer function  $\tilde{H}(\nu)$ , is  $V_i(\nu) = \tilde{H}(\nu) \tilde{V}_i(\nu)$ . The complex correlation function, at time lag  $\tau$ , of the two electric fields is:

$$\begin{aligned} R(\tau) &= \lim_{T \rightarrow \infty} \frac{4\pi^2}{2T} \int_{-\infty}^{+\infty} V_x(t) V_y^*(t - \tau) dt \\ &= \lim_{T \rightarrow \infty} \frac{4\pi^2}{2T} \int_{-\infty}^{+\infty} dt \int_{-\infty}^{+\infty} d\nu_x \int_{-\infty}^{+\infty} d\nu_y \int_{-\pi}^{\pi} d\theta \int_{-\pi}^{\pi} d\theta' \\ &\quad \times \tilde{E}_x(\theta, \nu_x) \tilde{E}_y^*(\theta', \nu_y) \tilde{H}_x(\nu_x) \tilde{H}_y^*(\nu_y) \tilde{G}_x(\theta, \nu_x) \tilde{G}_y^*(\theta', \nu_y) \\ &\quad \times e^{i(2\pi\nu_x t + \phi_x)} e^{-i(2\pi\nu_y(t - \tau) - \phi_y)} \quad (2) \end{aligned}$$

Remembering that  $\int_{-\infty}^{+\infty} e^{2\pi i t(\nu_x - \nu_y)} dt = \delta(\nu_x - \nu_y)$ , we obtain:

$$\begin{aligned} R(\tau) &= 4\pi^2 \int_{-\infty}^{+\infty} \int_{-\pi}^{\pi} \int_{-\pi}^{\pi} d\nu d\theta d\theta' \\ &\quad \times \tilde{\gamma}(\nu, \theta, \theta') \tilde{B}(\nu, \theta) \tilde{H}_x(\nu) \tilde{H}_y^*(\nu) e^{i(2\pi\nu\tau + \Delta\phi)} \quad (3) \end{aligned}$$

where:

$$\tilde{\gamma}(\nu, \theta, \theta') = \lim_{T \rightarrow \infty} \frac{1}{2T} [\tilde{E}_x(\theta, \nu) \tilde{E}_y^*(\theta', \nu)] \quad (4)$$

is the *source coherence function*,  $\Delta\phi = \phi_x - \phi_y$ , and

$$\tilde{B}(\nu, \theta, \theta') = \tilde{G}_x(\theta, \nu) \tilde{G}_y^*(\theta', \nu).$$

If, as is the case for POLAR,  $\tilde{G}_x(\theta, \nu) \simeq \tilde{G}_y(\theta, \nu) \equiv \tilde{G}(\theta, \nu)$ , then  $B(\nu, \theta) = |\tilde{G}(\theta, \nu)|^2$  is the power response function of the horn, or *beam pattern*. For a thermal source, such as the CMB,  $\tilde{\gamma}(\nu, \theta, \theta') = \tilde{\gamma}(\nu, \theta) \delta(\theta - \theta')$ . For POLAR  $\tilde{H}_x(\nu) \simeq \tilde{H}_y(\nu) \equiv \tilde{H}(\nu)$ , and only the real part of the complex correlation function is measured. Thus, POLAR's output can be expressed as:

$$\begin{aligned} R(\tau) &= 4\pi^2 \int_{-\infty}^{+\infty} d\nu \int_{-\pi}^{+\pi} d\theta \\ &\quad \times \tilde{\gamma}(\nu, \theta) \tilde{B}(\nu, \theta) |\tilde{H}(\nu)|^2 \cos(2\pi\nu\tau + \Delta\phi_\nu) \quad (5) \end{aligned}$$

where the  $\nu$  subscript on  $\Delta\phi$  incorporates a (potentially) frequency dependent phase shift between the two arms of the radiometer; see section 5.3. The properties of the source coherence function, the transfer functions, and the beam response completely determine the output voltage. Equation 5 will be useful in section 4 where POLAR's response to completely correlated, polarized signals produced by calibration sources is computed.

### 2.1. Minimum Detectable Signal

As in the case of the total power radiometer the sensitivity of the correlation polarimeter depends on both the system noise temperature and the RF bandwidth of the system. Since there are two RF amplifier chains the system temperature is their geometric mean:  $T_{sys} = \sqrt{T_{sys}^E T_{sys}^H}$ , and the minimum detectable signal in an integration time  $\tau$  is:

$$\Delta T = \sqrt{\frac{2T_{sys}^E T_{sys}^H}{\Delta\nu_{RF} \tau \cos^2 \Delta\phi}}, \quad (6)$$

where  $\Delta\nu_{RF}$  is the RF bandwidth, and  $\Delta\phi$  is the differential phase shift between the two arms prior to correlation (Thompson et al. 1998). Throughout this paper,  $E$  and  $H$  refer to the orthogonal polarization states separated by the OMT. Though not proven here, an intuitive way to obtain equation 6 comes from analysis of the radiometer signal-to-noise ratio for a fixed, small ( $T_{ant} \ll T_{rec}^{E,H}$ ) signal. The correlation polarimeter essentially differences the power (proportional to the system temperature) of each polarization state. Assuming the noise of the two receivers are uncorrelated (though approximately equal) then by propagation of errors it is seen that the RMS noise of the correlator output is  $\sqrt{2}$  higher than the noise of a single total power receiver with  $T_{sys}$ . Equation 6 is valid only when there are no RF gain or offset fluctuations. The effects of radiometer offset, stability, and other non-idealities are discussed in section 5.

## 3. THE POLAR RADIOMETER

POLAR's radiometer is comprised of three sections: 1) cold receiver components: optics, OMT, isolators, HEMT amplifiers, 2) room-temperature receiver components: warm RF amplifiers, heterodyne stage, warm IF amplifiers, band-defining filters, correlators, and 3) post-detection components: pre-amplifiers, low frequency processing, and data acquisition. In this section the details of the experimental design are presented. POLAR measures the  $U$  Stokes parameter, which is the real-part of the instantaneous cross-correlation of the electric fields in the E and H planes of the OMT. The OMT defines the  $x - y$  coordinate system of the antenna. The entire experimental apparatus rotates about the symmetry axis of the feed-horn in order to measure both linear polarization Stokes parameters. After a  $45^\circ$  rotation about the horn axis, the correlator gives an output proportional to the Stokes  $Q$  parameter. POLAR rotates continuously about the vertical at 2 RPM which sinusoidally modulates the output between  $U$  and  $Q$  at twice the rotation frequency:

$$I(\theta_t) = I_o + C \cos \theta_t + S \sin \theta_t + Q \cos 2\theta_t + U \sin 2\theta_t, \quad (7)$$

where  $\theta_t = 2\pi f t$ . In addition to the Stokes parameters  $Q$  and  $U$ , the terms  $C$  and  $S$  (which are synchronous with

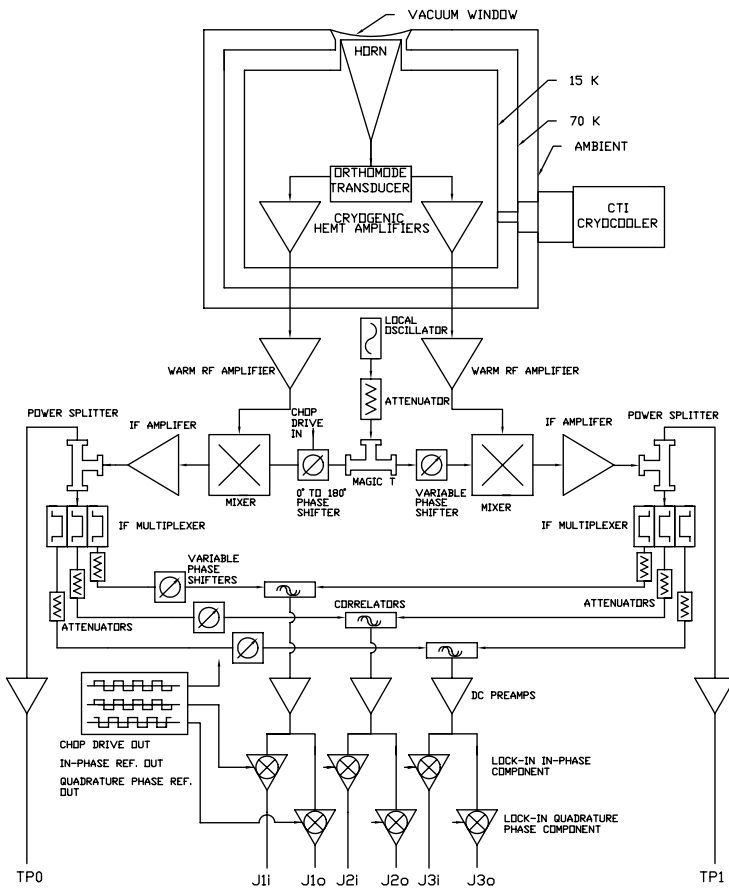


FIG. 2.— Schematic of the POLAR  $K_a$ -band correlation polarimeter.

the rotation at frequency  $f$ ) are monitored to determine our sensitivity to rotation-synchronous systematic effects, and to monitor atmospheric fluctuations. Phase sensitive detection at the modulation frequency removes an offset ( $I_0$ ) and other instrumental effects that are not modulated at this frequency.

### 3.1. Cryogenics

The dewar (figure 3) was custom fabricated<sup>6</sup> to house a cryocooler coldhead, and is large enough to accommodate possible upgrades including additional feed horns in the nominal 20 K (second stage) working volume. The first stage is used to cool a radiation shield, which is maintained at a nominal temperature of  $\sim 80$  K.

Following pump-down to  $\sim 1 \times 10^{-4}$  Torr, the pump is detached and the cryocooler's compressor (CTI 8500 Air Cooled) is activated. In the field it was found that the ultimate cold stage temperatures are correlated with the ambient temperature of the shelter in which POLAR resides. The compressor is air-cooled; water cooling was not possible due to the receiver's continuous rotation. The air cooling causes the compressor's compression ratio to be a strong function of ambient temperature, which modifies its cooling efficiency. Maintaining the temperature stability of the compressor is accomplished, to first order, by a commercial air-conditioner during the summer months

<sup>6</sup> Precision Cryogenic Systems: Indianapolis, IN

which counters the  $\sim 2$  kW heat output from the compressor. During the winter, the heat output by the compressor kept the enclosed POLAR shelter at a nearly constant temperature. The compressor is mechanically isolated from the radiometer by use of a separate rotation bearing coupled loosely to the motor-driven main bearing by copper braid (see figure 7). The compressor is further isolated on its bearing by use of rubber padding on all support structures.

The cold radiometer components are mounted on the 20 K stage, located inside the 80K stage radiation shield. Both waveguide outputs from the HEMTs connect to vacuum-tight WR-28 stainless steel waveguide feedthroughs<sup>7</sup> on the 300 K dewar wall. The feedthroughs are mounted on a single flange, which also serves as a feedthrough for the HEMT bias wiring and the temperature diode read-out wiring. The final major port in the dewar is the main vacuum optical window. This port is located  $\sim 3$  inches radially off the rotation axis of the cryostat to allow for additional feed horns at higher frequency.

### 3.2. Optics

POLAR's RF optical system is composed of a single corrugated feed horn. Due to the absence of supplemental beam-forming reflectors, cross-polarization of the instrument is near the minimum possible level for a millimeter wave receiver. POLAR's feed horn design is based on the procedure outlined in Zhang et al. (1993), and is similar to the  $K_a$ -band feed horn employed by the COBE DMR experiment (Janssen et al. 1979). The design goal of the

<sup>7</sup> Aerowave Corp., Medford, MA

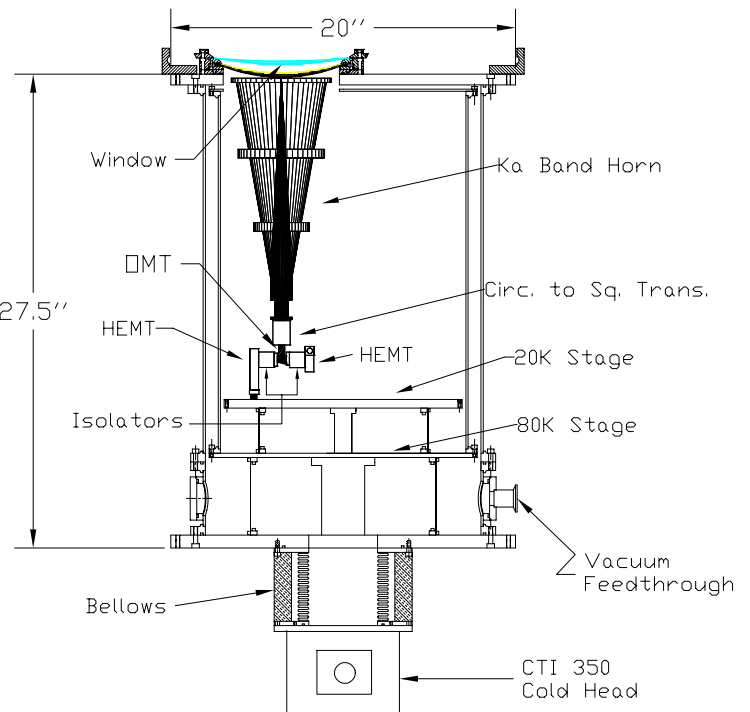


FIG. 3.— POLAR dewar and  $K_a$ -band cold receiver components. The horn is located off of the symmetry axis of the dewar in order to allow for future receivers to perform simultaneous observations. The HEMT outputs travel via stainless steel waveguides to a flange on the dewar bottom.

corrugated feed horn was to provide a low-sidelobe, low-cross-polarization, Gaussian beam on the sky across the full  $K_a$  band. The horn exhibits symmetry between its E and H planes and produces a diffraction-limited power response with a  $\simeq 7^\circ$  full-width-at-half-maximum (FWHM) across the band.

The beam pattern for the POLAR feed was computed using an 11 term Gauss-Laguerre model (Clarricoats & Olver 1984) to predict the far-field beam pattern out to  $\sim 20^\circ$ . A comparison of the measured and modeled beams is illustrated in figure 4. The simple Gauss-Laguerre model breaks down at low-power levels, which translates to the far off-axis response of the horn at  $\theta \geq 20^\circ$ . In the absence of a reliable model for the far off-axis behavior of our feed, we have measured the beam response for a variety of frequencies, for both polarizations, as well as the cross-polarization response (see figure 5).

The final component of the feed-horn is the mode converter, which is a separate electroformed element at the throat of the horn. The mode converter combines the  $TE_{11}^\circ$  and  $TM_{11}^\circ$  circular waveguide modes to create the hybrid  $HE_{11}^\circ$  corrugated waveguide mode. The mode converter's corrugations are of varying height, unlike those in the flare section of the horn. The primary purpose of the variable height corrugations is to define the bandpass of the horn, without sacrificing the side-lobe or cross-polarization levels achieved in the flare section of horn (Clarricoats & Olver 1984; Zhang et al. 1993). Following the throat in the optical path, there is an electroformed transition from the throat's circular output waveguide to the square-input waveguide of the OMT. This device was designed by matching the cutoff wavelengths of the  $TE_{10}^\square$  and the  $HE_{11}^\circ$  modes.

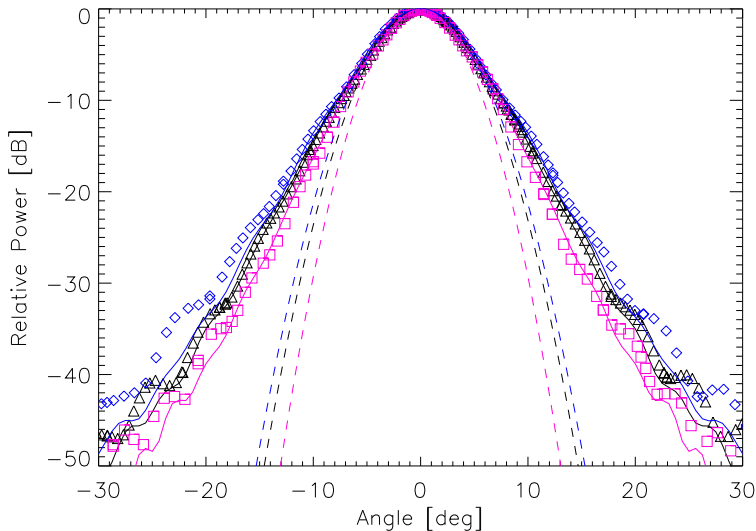


FIG. 4.— Gauss-Laguerre and Gaussian beam models compared to measured beam patterns. The diamonds (26 GHz), triangles (29 GHz), and squares (36 GHz) are the measured beam patterns in the E-plane. The solid lines represent the corresponding Gauss-Laguerre approximations, and the dashed lines are the best-fit Gaussians to the main beam of the measured data.

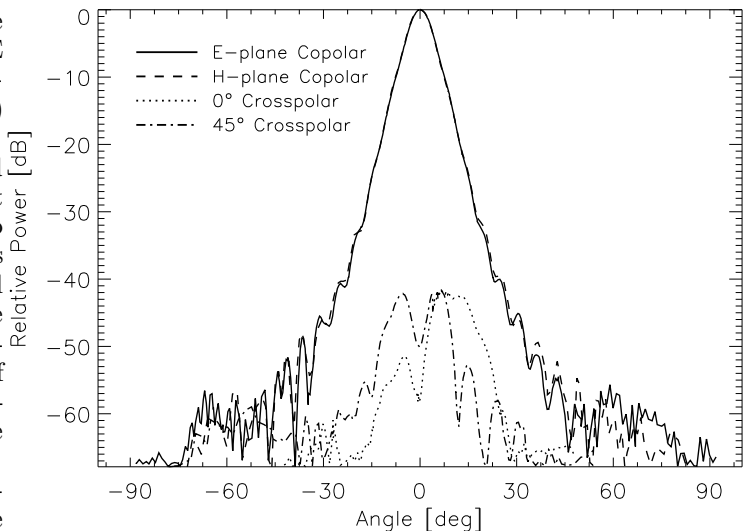


FIG. 5.— Beam maps of the feed-horn measured at 29 GHz are shown. The solid line is the co-polar E-plane power response pattern, the dashed line is the co-polar H-plane pattern, the dotted line is the E-plane cross-polarization response, and the dot-dashed line is the cross-polarization measured at  $45^\circ$  to the E-plane.

### 3.3. Orthomode Transducer

The orthomode transducer (OMT – variously referred to as a: polarization diplexer, dual-mode transducer, orthomode tee, and orthomode junction) is a waveguide device used to separate the two linear polarization states in the incident field. POLAR's OMT<sup>8</sup> is a three-port device with a square input port, and two rectangular output ports containing the orthogonal polarization signals.

The OMT's entrance port is  $K_a$ -band square guide which simultaneously supports both  $TE_{01}^\square$  and  $TE_{10}^\square$  modes. After the modes are separated by the OMT they are further isolated using cryogenic  $K_a$ -band isolators<sup>9</sup>. The isolators prevent coupling of the polarization states, which might occur from reflection by high-VSWR components further down the RF signal chain (such as the HEMT amplifiers). After leaving the OMT the fields in each of the two polarization states are processed (amplified, downconverted, and filtered) separately until correlation. POLAR's OMT can be described by a  $4 \times 4$  scattering matrix,  $\mathbf{S}_{ij}$ . Element 1 in the S-matrix refers to the input port with E-plane polarization while 2, 3, 4 refer to input H-plane, output E-plane, and output H-plane respectively. On-diagonal elements of  $\mathbf{S}_{ij}$  such as  $\mathbf{S}_{11}$  and  $\mathbf{S}_{22}$  define the return loss for input E-plane and H-plane polarization states. The terms  $\mathbf{S}_{13}$  and  $\mathbf{S}_{24}$  determine the co-polar transmission/forward loss, and are not necessarily equal. Differential loss (*e.g.*,  $\mathbf{S}_{13} \neq \mathbf{S}_{24}$ ) will lead to instrumental polarization and/or depolarization. The off-diagonal terms  $\mathbf{S}_{34} = \mathbf{S}_{43}$  characterize the output polarization isolation, and the terms  $\mathbf{S}_{14}$  and  $\mathbf{S}_{23}$  define the OMT's cross-polarization. Plots of the OMT performance are displayed in figure 13. As described in section 5, an offset in the output of the correlation polarimeter can be caused by either non-zero cross

<sup>8</sup> Atlantic Microwave: Bolton, MA, Model OM 2800

<sup>9</sup> Pamtech Corporation: Camarillo, CA

polarization or isolation.

### 3.4. Signal Processing

POLAR’s High Electron Mobility Transistor (HEMT) amplifiers (Pospieszalski 1992) are composed of four individual transistor stages. Each stage provides roughly 7-8 dB of gain, resulting in an overall gain of  $\sim 30$  dB. POLAR’s amplifiers utilize InP based devices for the first stage (which have lower noise-temperatures than GaAs devices) at the expense of slightly increased  $1/f$  noise. However, the low-frequency spectral properties of these amplifiers are largely irrelevant for correlation radiometers such as POLAR. POLAR’s two amplifiers have noise temperatures of  $\simeq 30$  K.

#### 3.4.1. Room Temperature Radiometer Box

After amplification by the cooled HEMT amplifiers, the RF signals are routed along a complicated, bending 3D path from the HEMTs to straight 6 inch long stainless steel waveguides which provide a thermal break from the 20 K HEMTs to the 300 K dewar walls. The stainless guides are bolted to the vacuum-tight WR-28 waveguide feedthroughs. Outside the dewar, straight sections of rhodium plated, brazed-copper waveguides are used to compensate for the path-length differences between the two polarizations incurred by the 3D bends. It is essential that the two signals traverse identical electrical path lengths so that the electric fields will be in-phase at the correlators. Finally, the waveguides enter the room temperature radiometer box (RTRB), where the signals are converted from waveguide to coax to match the inputs of the  $K_a$ -band warm HEMT amplifiers<sup>10</sup>. The noise temperatures of these devices are  $T_N \simeq 250$  K.

#### 3.4.2. Superheterodyne Components

Following the second-stage of amplification, the signals are down-converted in frequency from 26-36 GHz to 2-12 GHz by a 38 GHz local oscillator<sup>11</sup> (LO) and superheterodyne mixers<sup>12</sup>. The ultimate multiplication (correlation) of the coherent polarization signals is most easily performed at the lowest possible intermediate frequency (IF) band which preserves the nominal 10 GHz RF bandwidth. The IF spectrum is a (scaled) replica of the input RF band, with an identical bandwidth. Two stages of IF (2-12 GHz) amplification are used<sup>13</sup> to provide the appropriate bias power level into the multiplier. The gain of the IF amplifiers fall steeply above a frequency of  $f_{3dB} \simeq 12$  GHz, attenuating any residual out-of-band frequencies which might propagate in the coax transmission lines. Since each multiplier requires  $\sim 1$  mW of bias power, the IF signal must be amplified by  $\sim 60$  dB. After mixing and IF amplification the signals are divided into two paths. One path, referred to as the ‘total power detector’ channels (TP-E and TP-H) is detected by Schottky diodes<sup>14</sup>. ‘E’ and ‘H’ refer to the OMT port in which the respective total power signal originates. The other post-IF gain

path is sent into a frequency triplexer<sup>15</sup>. The function of the triplexers is three-fold. First they produce three (ideally) independent bands with which are used to investigate the spectral behavior the data. Secondly, these devices allow us to flatten the gain of the system across the wide RF-bandwidth provided by the HEMTs. Finally, the differential phase between the two arms can be made flatter across the sub-bands than across the full RF band. Prior to correlation the gain and phase of each sub-band are matched with fixed attenuators and phase shifters.

#### 3.4.3. Correlators

There are several correlator designs used in correlation radiometers. POLAR’s correlator is a Schottky-diode mixer<sup>16</sup>. A mixer-based correlator is composed of a double balanced mixer, a phase modulating element, and lock-in detection. The correlator is a wide-band double-balanced analog multiplier. This type of multiplier isolates both RF input ports from one-another, while the IF port is coupled to both. The primary difference between a multiplier and a conventional mixer is that the IF bandwidth of the multiplier is made intentionally narrow to suppress frequency components greater than  $\sim 100$  MHz, and the output of the multiplier can support DC. Narrow RF-band multipliers are often used as phase detectors.

The multipliers are double balanced mixers with RF band passes from 1-12 GHz and an IF bandpass from 0-500 MHz. The IF output port is not transformer-coupled, and can thus propagate the DC signal proportional to the correlation between signals in the  $x$  and  $y$  polarization states. Phase modulation and phase-sensitive detection (PSD) is accomplished by an electronic  $0^\circ - 180^\circ$  phase shifter<sup>17</sup>, and a switch-referenced synchronous demodulator<sup>18</sup> and integrator. The phase of the LO is switched between  $0^\circ$  and  $180^\circ$  at 1 KHz prior to mixing the  $E_y^{RF}$  waveform. The voltage produced by the correlators at this stage thus switches between  $\kappa E_x^{RF} E_y^{RF}$  and  $-\kappa E_x^{RF} E_y^{RF}$  at 1 KHz, where  $\kappa$  is the intensity-to-voltage conversion factor. The output of the lock-in detectors is proportional only to the correlated component in each arm of the polarimeter.

Two lock-in detectors per correlator are used; one in-phase with the phase shifter modulation, and the other for the quadrature-phase component. The latter are referred to as quadrature phase channels (QPC), and are used as noise monitors as discussed below. The QPC are powerful monitors of the noise and potential systematic effects of the correlator channels. A custom lock-in detector circuit was constructed for each correlator channel. Signals leave the pre-amp card and enter a separate RF-tight box containing six separate lock-in circuits, corresponding to phase sensitive detection of three correlators, each with two reference phases, ‘in-phase’ and ‘quadrature-phase’. The demodulated signal is low-pass filtered at 5 Hz.

#### 3.4.4. Electronics Box and Housekeeping

Thermal regulation of the RTRB is essential to the stability of the instrument over long periods of time. The

<sup>10</sup> MITEQ: Hauppauge, NY, Model JS426004000-30-8P

<sup>11</sup> Millimeter Wave Oscillator Co.: Longmont, CO

<sup>12</sup> MITEQ: Model TB0440LW1

<sup>13</sup> MITEQ: Model AFS6-00101200-40-10P-6

<sup>14</sup> Hewlett Packard: Model HP 8474C

<sup>15</sup> Reactel Corp.: Gaithersburg, MD

<sup>16</sup> MITEQ: Model DBP112HA

<sup>17</sup> Pacific Millimeter Products: Golden, CO

<sup>18</sup> Analog Devices: Model AD 630

most temperature sensitive components are the non-linear devices such as the mixers, multipliers, and especially the Gunn oscillator. To regulate the temperature, a thermal control circuit which employs feedback from a sensor inside the RTRB was constructed. This control circuit is centered on a commercial microprocessor-based PID controller<sup>19</sup>, and can regulate up to 300W of power applied directly to six 25 W heater pads<sup>20</sup>. The power and control of our approach allows us to regulate the temperature of all elements in the RTRB to better than 100 mK<sub>RMS</sub>.

Several other housekeeping signals, including temperature sensor diodes inside the cryostat (on the HEMTs, 20 K cold plate, and feed horn) and the dewar pressure are monitored. A multi-stage power regulation approach is implemented. This system employs precision voltage regulators and references throughout the RTRB; all signal circuitry (HEMT bias cards, post-detection electronics, etc.) are voltage regulated and EMI shielded.

### 3.4.5. Post-Detection Electronics

The pre-amplifier is the final component of the signal chain for the total power detectors, and the penultimate component for the correlators (as these are post-detected via the lock-in circuits described above). To minimize the susceptibility to electromagnetic interference (EMI), the signals are amplified and filtered before leaving the radiometer box. A single circuit board contains five (two total power channels, three correlator channels) circuits. The card is mounted in close proximity to the correlators and shares the same thermally regulated environment. The first stage of the post-detection electronics is an adjustable gain low noise pre-amplifier. Following the gain stage is a 4-pole, 5Hz anti-aliasing filter<sup>21</sup>. The bandpass of the anti-aliasing filter also serves to set the fundamental integration time,  $\tau$ .

### 3.4.6. Data Acquisition

The data acquisition system is composed of an analog-to-digital converter<sup>22</sup>, and a Pentium II notebook computer running National Instruments Labview software. The analog-to-digital converter (ADC) samples all 8 data channels as well as 8 housekeeping channels at 20 Hz. By digitizing all of the data in close physical proximity to the detectors, the potential for EMI contamination is minimized. The data files are indexed by calendar time and date, with several hundred files stored per day. After 7.5 minutes of acquisition, the data files are transferred from the notebook computer (located on the rotation platform) to a desktop computer via a local area network Ethernet connection. The coax Ethernet connection leaves the rotating electronics box through 2 channels of a 10 channel shielded slip-ring.

### 3.5. Vacuum Window

A multi-element vacuum window (figure 6) is composed of a 0.003 inch vacuum-tight polypropylene vacuum barrier and a 0.125 inch (permeable) Gore-Tex<sup>23</sup> layer which

<sup>19</sup> Omega Inc.: Stamford, CT

<sup>20</sup> MINCO: Minneapolis, MN

<sup>21</sup> Frequency Devices: Haverhill, MA

<sup>22</sup> National Instruments DIO-MIO-16 Daqpad

<sup>23</sup> W.L. Gore & Associates: Newark, DE

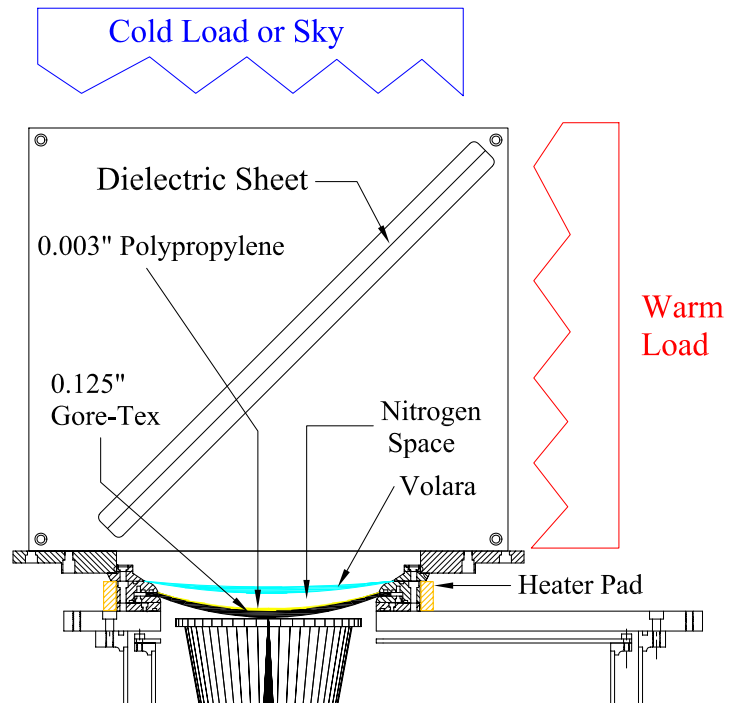


FIG. 6.— Side view of window and calibrator configuration. The calibrator grids (either the wire grid or the dielectric sheet) mount on a rotation bearing attached to the window flange. The calibrators fill the beam and rotate around the horn axis. For both the dielectric sheet and the wire grid calibrators, hot and cold loads are used to generate  $\sim 100\%$  polarized sources, ranging from 20 mK (dielectric sheet) to 200 K (wire grid).

supports the atmospheric load on the window. A layer of Volara<sup>24</sup> (expanded polyethylene) seals in a dry-nitrogen gas layer between the polypropylene and prevents condensation and ice on the vacuum window. A resistive heater element wrapped around the vacuum window flange warms the window to reduce the formation of dew. With this window the dewar pressure remains below  $10^{-6}$  Torr for months at a time. The emission from the window is estimated to be  $\lesssim 20$  mK, and the reflection amplitude coefficient is  $\lesssim 10\%$ .

### 3.6. Ground Screens

POLAR uses two concentric ground screens; one co-rotating with the receiver, the other fixed to the observatory structure (see figure 7). The use of two ground screens is not unusual in the field, although POLAR's screens are designed to reject polarized beam spillover, rather than unpolarized, total-power spillover. The inner ground screens are designed to terminate the side-lobe power in a well-known and constant temperature source, and absorb, rather than reflect, solar and lunar light. This method reduces the amount of radiation polarized by reflection. The inner conical ground screen is covered with 0.5 inch Eccosorb foam<sup>25</sup>. This absorptive approach is uncommon in CMB anisotropy experiments as it increases the total power loading on the detectors. However, the increase in system temperature due to the inner shield is estimated to be  $\lesssim 1$ K. Polarization generated by emission or reflection from the

<sup>24</sup> Voltek Corp.: Lawrence, MA

<sup>25</sup> Emerson & Cuming: Randolph, MA, Product LS-26

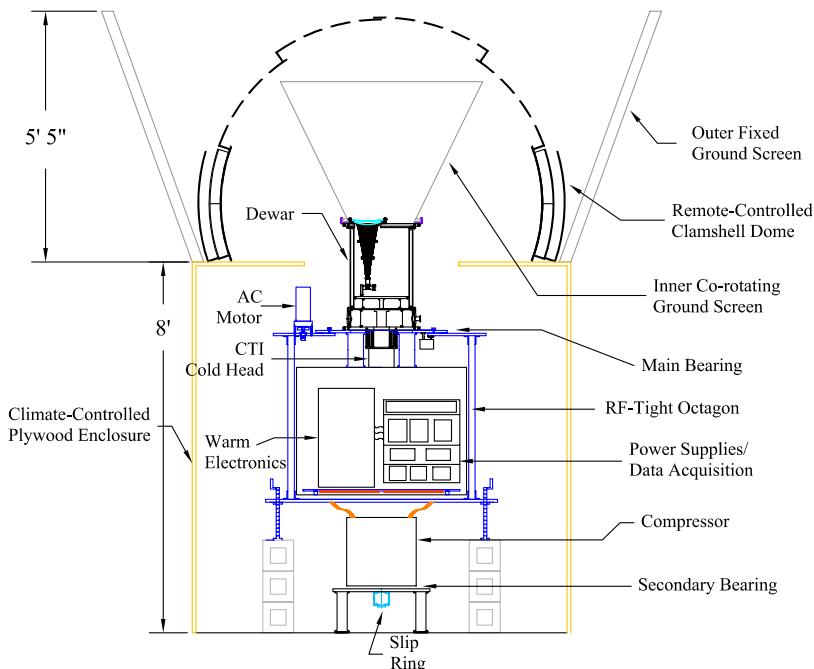


FIG. 7.— POLAR observatory and ground screens. Two sets of ground screens are used to reduce the polarized spillover from the earth, as well as polarized emission from the shields themselves. The outer shield is fixed to the structure in which POLAR resides, and is composed of a lightweight steel skeleton covered by 0.05" aluminum sheets. The inner ground screen is covered with flat Eccosorb panels, and co-rotates with the radiometer. Also shown is the motor-driven, fiberglass clamshell-dome which is remotely operated via the World Wide Web in the event of inclement weather. The rotation mount, drive motor, bearing, and angular encoder are also shown.

bare metal surface of an uncovered shield would be more troublesome than the slight increase in system temperature. Since the inner ground screen co-rotates with the receiver, it will only produce a constant offset to which the instrument is insensitive. The second level of shielding is of the more conventional reflective-scoop design, *e.g.* Wollock et al. (1997). The scoop is mounted to the side of the POLAR observatory, and is made of four aluminum panels, 8' wide and 4.8' high. The level of sidelobe suppression is estimated using Sommerfeld's scalar diffraction theory for points deep in the shadow region of a knife-edge scatterer (Jackson 1975). The estimated suppression is  $\approx -40$  dB, which in combination with a similar (measured) figure from the inner ground screen, and the sidelobe response of our feed horn, gives a total estimated sidelobe suppression better than  $-100$  dB. The response at  $90^\circ$  off-axis relative to the peak forward gain was measured to be  $< -50$  dB using a polarized source transmitting in the  $K_a$ -band from various locations around the instrument enclosure. As discussed in section 5.4, the square shape of the scoop is thought to have produced a  $\sim 100 \mu\text{K}$  offset in the Stokes parameters.

### 3.7. Rotation Mount and Drive System

Measurement of the Stokes parameters is dependent on signal modulation under rotation and employs a 30 inch diameter bearing and AC motor system to rotate the cryostat at 2 RPM ( $\sim 33$  mHz). An AC motor produced smoother motion than several stepper motors tried ini-

tially, and was chosen for continuous rotation. The dewar rides on a bearing composed of two plates each with a 0.100 inch wide channel filled with  $\sim 400$  stainless-steel ball-bearings. The motor pulley has a relative angle encoder which reads out the rotation angle. In addition, a one-bit absolute encoder is triggered once per revolution at a specific angular position which defines the zero angle of the instrument frame. In order to decouple the vibrations produced by the cryocooler compressor from the receiver, a separate, vibration isolated rotation mount is used to support the compressor. The second bearing is loosely coupled to the main rotation bearing/AC motor drive using braided copper straps. Power and ethernet connections interface with the rotating system via the 10 channel slip ring. The mount is not steerable, so POLAR is restricted to zenith scans.

### 3.8. Instrument Bandpasses

Laboratory measurement of the room temperature radiometer box bandpasses used an HP 83751A Synthesized Sweeper to produce a swept signal from 13 to 18 GHz, which was subsequently doubled in frequency by an active doubler (producing 26 - 36 GHz) and fed into a power splitter. The outputs from the power splitter were 100% correlated, and these signals were fed into the waveguide input ports of the RTRB. The correlated signals were attenuated to provide a power level similar to that obtained when viewing the sky. The bandpasses of the three correlator channels are shown in figure 8.

### 3.9. Receiver Noise and Sensitivity

There are several methods to compute the noise temperature of a correlation radiometer. Y-factor measurements (Pojar 1990) of the total power channels were performed with both a cooled internal calibrator (which is accurate, but does not include the effects of the feed-horn) and an

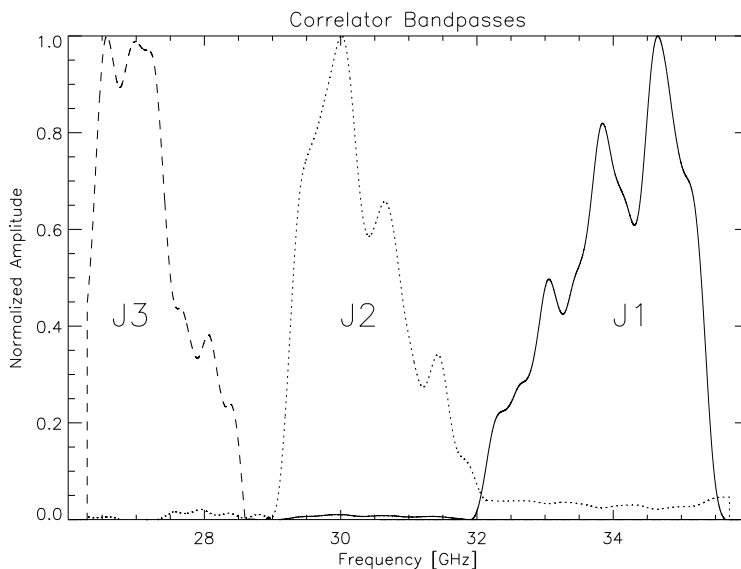


FIG. 8.— Bandpasses of all three correlator channels are shown, not including the HEMT amplifier response. A  $K_a$ -band correlated signal is injected into each arm of the warm electronics, and the signal frequency is swept from 26 to 36 GHz to measure the bandpasses.

ambient temperature external load (which is faster, but requires a larger dynamic range) to ensure consistency. The ambient temperature loads used were 300K, 77K, and the sky ( $\simeq 12$ K, zenith).

In addition to the  $y$ -factor method  $T_{rec}$ , was inferred from noise measurements. Given the instrument bandwidth  $\Delta\nu$ , the voltage fluctuations  $\Delta V_{rms}$  in an integration time  $\tau$ , and the calibration coefficient,  $g$  in [V/K], the noise temperature of the receiver can be estimated using the radiometer equation:

$$T_{rec} = \frac{g^{-1}}{\kappa} \Delta V_{RMS} \sqrt{\Delta\nu\tau} - T_{load}, \quad (8)$$

where  $\kappa = 1$  for the total power channels, and  $\kappa = \sqrt{2}$  for the correlator channels. For both the total power channels and the correlators  $\Delta T_{rms}$  is a linear function of the load temperature. The  $x$ -intercept of these lines is equal to the negative of the system noise temperature.

The system noise temperature is dominated by the noise temperature of the HEMT amplifiers. However, the contribution of the room-temperature amplifiers, as well as loss in components preceding the HEMTs, cannot be neglected. The dominant lossy elements preceding the HEMTs are the cryogenic isolators and the dewar's vacuum window. The isolators' exact physical temperature is unknown, but estimated to be  $\lesssim 40$ K, which is the physical temperature of the horn, so this is a worst-case estimate. Their insertion loss is 0.1 dB. The loss of the vacuum window is conservatively estimated at 1%. The room temperature RF amplifiers have noise temperatures of 232 K. The total estimated system noise temperature including all factors is  $T_{sys} = 46$  K. Table 1 displays the noise temperatures of all channels using the linear intercept method outlined above. Some compression was discerned for the highest ambient temperature load used (300 K). Correlator J3 exhibits the highest level of compression and not coincidentally, obtains the highest NET.

#### 4. CALIBRATION

An accurate calibration is essential to the success of the POLAR experiment. An ideal source would be a polarized astrophysical point source with enough power to be seen in "real-time". For illustration, we compute the power needed to produce a  $5\sigma$  detection in a 1 second integration – bright enough to detect in real-time. The antenna temperature seen by POLAR's total power detectors when viewing a source of flux density  $S_\nu$  is  $T_{ant} = 2.8 S_\nu \frac{\mu\text{K}}{\text{Jy}}$ . POLAR's NET  $\simeq 1$  mK  $s^{1/2}$ , so a source of antenna temperature  $T_{ant} \simeq 5$  mK is required for a  $5\sigma$  detection in one second. This is equivalent to a  $\sim 1700$  Jy source. For comparison, Cas-A, the brightest known radio source, has a flux density of only  $194 \pm 5$  Jy at 32 GHz (Mason et al. 1999). Since Cas-A is less than 10% polarized at 32 GHz, the polarized signal is smaller still. Clearly, no astrophysical sources were suitable for POLAR's calibration. In addition, the rotation mount is not pointable, so POLAR can only observe sources at zenith transit. Instead, polarized signals were created by reflection of black-body emission from wire grids (in-laboratory calibration) and dielectric sheets (during observing campaign).

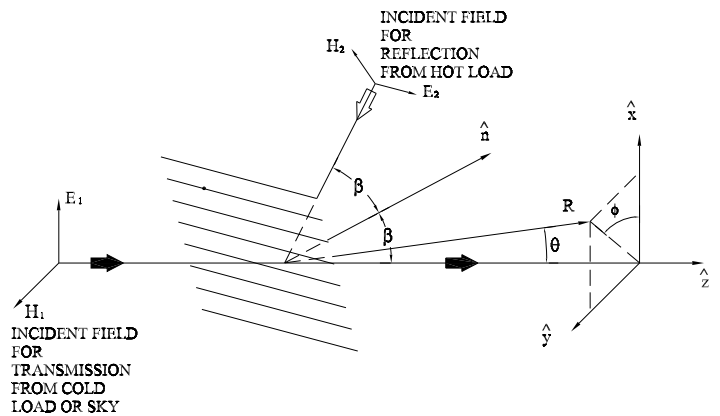


FIG. 9.— Geometry of the Wire Grid Calibrator. For both the wire grid calibrator and the dielectric sheet calibrator,  $\beta = 45^\circ$ , and  $\theta = 0^\circ$ . See figure 10 for an example calibration run.

#### 4.1. Wire Grid Calibrator

Two methods of calibration were used, depending on the dynamic range required for the measurement. Initially, a wire grid was used to test the receiver in the lab and to probe instrumental polarization and cross-polarization behavior. The grid produces a highly polarized ( $> 99\%$ ), bright ( $T_{ant} = 200$  K) signal. The limited dynamic range of the receiver does not allow the wire grid to be used as a calibrator when the instrument is in its observing (highest gain) configuration. However, the grid was extremely useful for characterizing the polarimetric fidelity of the receiver.

Wire grid calibrators (WGC) are useful for near field polarization calibration (Lubin & Smoot 1981; Gasiewski & Kunkee 1993; Chu 1975). The WGC is a passive source which provides correlated electromagnetic fields in each arm of the receiver, and is placed outside the cryostat for rapid implementation. The grid (figure 9) transmits thermal radiation from a black-body source in one polarization, and reflects thermal radiation from a second black-body source (at a different temperature) into the orthogonal polarization. For the POLAR calibrator, the cold load is located above the grid and produces fields  $E_1$  and  $H_1$ , and the warm load produces fields  $E_2$  and  $H_2$ . Ideally,  $H_1$  is transmitted and  $E_2$  is reflected into the feed-horn producing a  $\simeq 100\%$  polarized diffuse source with an antenna temperature approximately equal to the thermodynamic temperature difference between the two loads.

The wire-grid calibrator was fabricated by deposition of copper onto a 0.002 inch mylar substrate. The wires are 0.008 inch wide with 0.008 inch spaces. For support the grid is sandwiched between Dow Corning "pink" Styrofoam sheets (emissivity  $\leq 1\%$ ), and the sandwich is mounted at  $45^\circ$  to the aperture plane (figure 6). The grid has an integrated bearing system which allows it to rotate directly over the vacuum window.

The correlator output voltage depends on the coherence of the electric fields produced by the thermal radiators. However, only the antenna temperatures of the hot and cold loads are known, not the electric fields produced in the  $x$  and  $y$  directions. Fortunately, as shown below, only the antenna temperatures are needed. The field input to the feed-horn is  $\vec{H}_1 + \vec{E}_2$ . In terms of the  $(x', y')$  basis of the

feed-horn and OMT and the  $(x, y)$  basis of the rest frame of the WGC, the magnitude of the electric field produced by the WGC as the polarimeter is rotated by an angle  $\alpha$  is:

$$\begin{aligned} E_{x'} &= E_x \cos \alpha + E_y \sin \alpha \\ E_{y'} &= -E_x \sin \alpha + E_y \cos \alpha. \end{aligned}$$

Since the load completely fills the antenna beam, the output of the correlator from the coherence function given by equation 5 is:

$$\begin{aligned} V_{out} &\propto \langle \hat{E}_{x'}(\nu) \tilde{E}_{y'}^*(\nu) \rangle \\ &= \langle (E_x \cos \alpha + E_y \sin \alpha)(-E_x^* \sin \alpha + E_y^* \sin \alpha) \rangle, \end{aligned}$$

where the fields  $E_x, E_y$  produced by the loads are given by:

$$\begin{aligned} E_y &= E_{y_o} \cos[\nu t + \phi_y(t)] \\ E_x &= E_{x_o} \cos[\nu t + \phi_x(t)], \end{aligned}$$

we obtain:

$$\begin{aligned} V_{out} &\propto \langle -E_x \cos \alpha E_x^* \sin \alpha + E_y \sin \alpha E_y^* \sin \alpha \rangle \\ &= \langle E_y E_y^* - E_x E_x^* \rangle \sin \alpha \cos \alpha \\ &= Q \sin 2\alpha = \gamma(T_y - T_x) \sin 2\alpha \end{aligned}$$

where  $\gamma$  converts antenna temperature (measured by the radiometer) to intensity (the units of the Stokes parameter,  $Q$ ). Note that at  $\alpha = 0^\circ, 90^\circ, 180^\circ, 270^\circ$  the correlators have zero output as the fields are completely aligned along one axis of the OMT. Ideally, the grid would reflect  $T_{hot}$  from the side in 100% horizontal polarization and transmit  $T_{cold}$  from the top in 100% vertical polarization, resulting in

$$V_{out} \propto \gamma(T_{cold} - T_{hot}) \sin 2\alpha. \quad (9)$$

In practice, due to loss and reflection, the following antenna temperatures are observed at the feed-horn in the two orthogonal polarizations (Gasiewski & Kunkee 1993):

$$\begin{aligned} T_{hot'} &= r_{||}[(1 - r_l)T_{hot} + r_l T_{bg}] + \\ &\quad (1 - r_{||})[(1 - r_l)T_{cold} + r_l T_{bg}] \quad (10) \\ T_{cold'} &= t_{\perp}[(1 - r_l)T_{cold} + r_l T_{bg}] + \\ &\quad (1 - t_{\perp})[(1 - r_l)T_{hot} + r_l T_{bg}], \end{aligned}$$

where  $r_{||}$  is the grid reflection coefficient for radiation polarized parallel to the wires,  $t_{\perp}$  is the grid's transmission for radiation polarized perpendicular to the wires,  $r_l$  is the reflection coefficient of the load, and  $T_{bg} = T_{hot}$  is the effective background temperature surrounding the calibrator. In the above equations, the effects of the emissivities and dielectric constants of the mylar and Styrofoam have been neglected.

Two pairs of temperature differences were used to characterize POLAR. Using a 300 K load (in reflection) and the sky (in transmission) a polarized antenna temperature of 256 K is obtained. Using a 300 K load (in reflection) and a 77 K Liquid Nitrogen load (in transmission) an antenna temperature of 196 K is obtained. The the following properties of the grid were assumed: parallel polarization reflectivity  $r_{||} = 0.995$ , perpendicular polarization transmissivity  $t_{\perp} = 0.95$ , load reflectivity  $r_l = 0.02$ . A plot of a calibration run is shown in figure 10. The sinusoidal oscillations are the result of rotation of the grid over the feedhorn. The first set of oscillations corresponds to the 300 K load and the sky and the second set corresponds to 300 K load and the 77 K liquid nitrogen load.

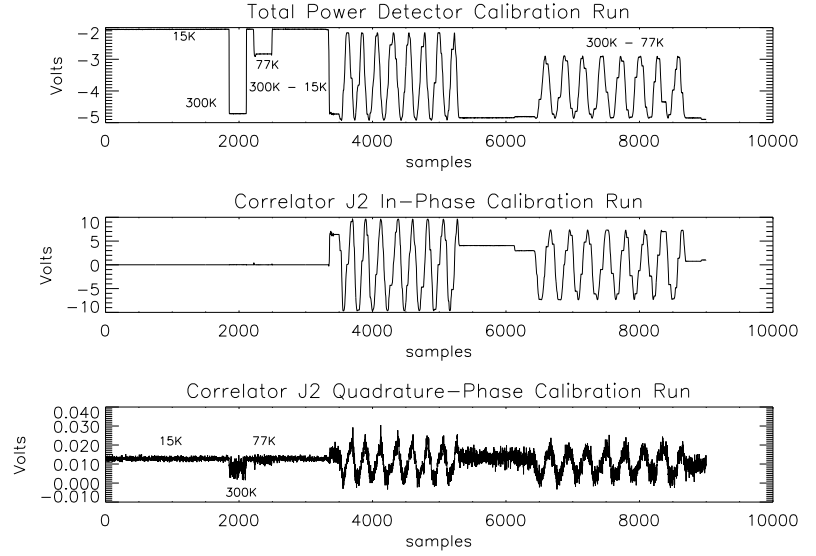


FIG. 10.— Voltages out of correlator J2 and total power detector TP-E (top figure) during calibration with the wire grid calibrator are displayed. Output from TP-E is  $90^\circ$  out of phase with respect to the correlator channels. TP-E uses a negative polarity total power detector. The middle figure shows the voltage out of J2's in-phase lock-in detector, the bottom figure show the corresponding voltage out of J2's quadrature phase lock-in detector. The IPC and the QPC have the same gain. The various temperature loads are indicated at the time they are applied. The first set of oscillations corresponds to a polarized signal obtained using a 300 K load (reflected) and the sky (transmitted), which produces a  $\sim 260$  K signal. The second set of oscillations corresponds to a polarized temperature obtained by using a 300 K load and a liquid nitrogen load producing a  $\sim 190$  K signal. The output of the quadrature phase detector is suppressed by  $\sim 30$  dB relative to the in-phase channel. The noise envelope of the J2 QPC detector is a function of the load temperature, and is used as a noise monitor.

#### 4.1.1. Gain Matrices

Following Gasiewski & Kunkee (1993) the output of the polarimeter versus rotation angle is modelled as a linear combination of the Stokes parameters at the feed horn. The output voltage is modelled as a vector  $\bar{v}$ :

$$\bar{v} = \begin{pmatrix} v_y \\ v_x \\ v_Q \end{pmatrix} = \begin{pmatrix} g_{yy} & g_{yx} & g_{yQ} \\ g_{xy} & g_{xx} & g_{xQ} \\ g_{Qy} & g_{Qx} & g_{QQ} \end{pmatrix} \begin{pmatrix} T_{Fy} \\ T_{Fx} \\ T_{FQ} \end{pmatrix} + \begin{pmatrix} o_y \\ o_x \\ o_Q \end{pmatrix} + \bar{n} \quad (11)$$

or

$$\bar{v} = \hat{\mathbf{g}} \bar{T}_f + \bar{o} + \bar{n} \quad (12)$$

where  $\hat{\mathbf{g}}$  denotes the gain matrix,  $(\bar{T}_f)$  is the vector of input antenna temperatures produced by the grid, and  $\bar{o}$  and  $\bar{n}$  represent offset and noise contributions to  $\bar{v}$  respectively. Ideally,  $\hat{\mathbf{g}}$  would have only on-diagonal elements. The off-diagonal elements of  $\hat{\mathbf{g}}$  correspond to various non-idealities of the instrument which will result in offsets in our measurements. We will elaborate on these terms in the following.

In practice, the grid is placed directly over the feed-horn aperture formed by the vacuum window and rotated while the polarimeter is held fixed. The resulting vector of voltages is recorded and a least-squares fit is made to the data using the radiometer model of equation 11. The gain matrix parameters, including the off-diagonal cross-talk elements, and the offsets are recovered for each calibration run. With the antenna temperatures of the loads given

by equation 10, the voltages out of the two total-power channels and the correlator channel are:

$$\begin{aligned} \bar{v} &= \begin{pmatrix} v_y(\alpha) \\ v_x(\alpha) \\ v_Q(\alpha) \end{pmatrix} \\ &= \begin{pmatrix} g_{yy}T_c + g_{yx}T_s + g_{yQ}(T_{hot'} - T_{cold'}) \sin 2\alpha + o_y \\ g_{xy}T_c + g_{xx}T_s + g_{xQ}(T_{hot'} - T_{cold'}) \sin 2\alpha + o_x \\ g_{yQ}T_c + g_{xQ}T_s + g_{QQ}(T_{hot'} - T_{cold'}) \sin 2\alpha + o_Q \end{pmatrix} + \bar{n} \end{aligned} \quad (13)$$

where

$$T_c = T_{hot'} \cos^2 \alpha + T_{cold'} \sin^2 \alpha$$

and

$$T_s = T_{hot'} \sin^2 \alpha + T_{cold'} \cos^2 \alpha.$$

To recover  $\hat{\mathbf{g}}$ , we first integrate long enough that the noise term,  $\bar{n}$ , is negligible, and then measure the offsets,  $\bar{o}$ . Then equation 13 is inverted to obtain  $\hat{\mathbf{g}}$ . The on-diagonal elements ( $g_{xx}, g_{yy}, g_{QQ}$ ) of  $\hat{\mathbf{g}}$ , dominate the matrix; they are the terms which measure the system calibration in [V/K]. Typical values are  $\sim 100$  K/V. The off-diagonal elements are equally important as they encode the system's gain imbalance, cross-talk, and imperfect isolation between polarization states. The  $g_{xy}$  terms are approximately 1% of the  $g_{xx}, g_{yy}$  terms, and the  $g_{xQ}, g_{yQ}$  terms are  $\leq 1\%$  of the  $g_{QQ}$  terms for all three correlators. These effects lead to offsets, and may be incorrectly interpreted as celestial signals if they are not removed or are unstable in time.

There are two independent effects responsible for the off-diagonal elements, corresponding to the two different off-diagonal elements  $g_{xy} = g_{yx}$  and  $g_{xQ} = g_{yQ}$ . To analyze the effects of  $g_{xy} \neq 0$ , we set  $g_{yQ} = n_y = o_y = 0$ , and identify the first non-ideality,  $g_{xy}$  (which is equal to  $g_{yx}$ ). This implies that at  $\alpha = 0$ , when only  $T_{hot'}$  should be observed,  $v_y = g_{yy}T_{hot'} + g_{yx}T_{cold'}$  is observed. Thus,  $g_{xy}$  terms represents cross-polarization between the orthogonal polarizations. The main contribution to the correlator offset is from cross-polarization of the OMT and/or imperfect isolation of the OMT. The off-diagonal elements, *e.g.*,  $g_{xQ}$ , are attributed to gain differences in the feed horn's E and H plane power response, and can be equalized in hardware and/or calibrated out in software.

Since two pairs of temperature differences (300 K load vs. 77 K load and 300 K load vs. the sky) were used, the calibration constants as a function of the temperature difference were measured and checked for linearity. The two pairs of loads produced effective polarized antenna temperatures of 256 K and 196 K, and it was verified that the calibration constants were equal to better than 10% over this range.

#### 4.2. Dielectric Sheet Calibrator

As mentioned above, calibrations performed during the observing campaign did not use the wire grid calibrator. The primary reason for this was the limited dynamic range of the polarimeter; both the last stage of IF amplifiers and the correlators themselves began compressing when the antenna temperature was  $\sim 100$  K. When the sky was the cold load, a full rotation of the wire grid produces a modulated signal with amplitude  $100 \text{ K} < T_{\text{ant}} < 250 \text{ K}$ . The variation in bias power to the correlators produced

by the WGC as it was rotated was significant. The largest imbalance loaded the correlators with 40 K on one port and up to 290 K on the other port. This imbalance is undesirable and was another reason the Dielectric Sheet Calibrator (DSC) was used (O'Dell et al. 2002). During observations, the calibrator should produce a total power load similar to the sky loading, which is only slightly polarized. This avoided compression in the IF amplifiers and/or the correlators, and had the added virtue of more closely approximating the faint polarized signal that we sought to measure. During the observing campaign, the wire grid calibrator was replaced by a thin (0.003 inch) polypropylene film. This produces a signal that is only partially polarized. The polarized signal produced by the (DSC) is

$$Q = [(T_{hot} - T_{cold})(R_{TE} - R_{TM}) + (T_S - T_{cold})(\epsilon_{TE} - \epsilon_{TM})] \cdot \sin 2\alpha \quad (14)$$

where  $T_S$  is the physical temperature of the dielectric sheet, and  $\epsilon_{TE}$  ( $\epsilon_{TM}$ ) is the emissivity of the dielectric in the TE (TM) polarization state. Note that this expression reduces to equation 9 in the wire grid case, where  $R_{TE} - R_{TM} = 1$ , and  $\epsilon_{TE} = \epsilon_{TM} = 0$ .

The reflection coefficients of the DSC is determined by the dielectric constant and the geometry:

$$R = \frac{[\cos^2 \theta - \gamma^2]^2 \sin^2 \delta}{4\gamma^2 \cos^2 \theta \cos^2 \delta + [\cos^2 \theta + \gamma^2]^2 \sin^2 \delta} \quad (15)$$

where  $i \in \{TE, TM\}$ , and

$$\gamma_{TE} \equiv \sqrt{n^2 - \sin^2 \theta} \quad (16)$$

$$\gamma_{TM} \equiv \frac{1}{n^2} \sqrt{n^2 - \sin^2 \theta} \quad (17)$$

$$\delta = 2\pi ft \sqrt{n^2 - \sin^2 \theta}, \quad (18)$$

where  $n$  is the refractive index of the sheet,  $f$  is the frequency,  $t$  is the sheet thickness, and  $\theta$  is the angle of incidence of the incoming radiation. For our geometry,  $\theta = 45^\circ$ .

For 0.003 inch polypropylene at 30 GHz,  $R_{TE} - R_{TM} \approx 0.2\%$ . The emission from the sheet is  $\sim 4$  mK per 0.001 inch of thickness, and is negligible compared to the reflection-induced signal. When the sky is used as the cold load and a 300 K hot load is used,  $T_{hot} - T_{cold} \approx 260\text{K}$ , and produces a rotation modulated polarized calibration signal of  $\sim 500$  mK, and an unpolarized background power of  $\sim 10$  K (the sky temperature).

Equation 15 was verified in laboratory tests; the results for 0.003 inch polypropylene are given in Figure 11. The primary source of error in our final calibration was the slight thickness variations in the sheet; these 5% variations lead to a final calibration error of  $\sim 10\%$ .

## 5. SYSTEMATIC EFFECTS AND RADIOMETRIC OFFSETS

### 5.1. System Sensitivity Degradation

Once the conversion between voltage and temperature is known, by measuring the voltage RMS the temperature RMS can be obtained. The noise in an arbitrary integration time,  $\tau$ , is  $\Delta T_{RMS} = \text{NET}/\sqrt{\tau}$ . Again, the model of the noise of the total power detectors differs from that of the correlators. For the Total Power detectors

$$\text{NET}^{\text{TP}} = \frac{T_{\text{rec}} + T_{\text{load}}}{\sqrt{\Delta\nu}},$$

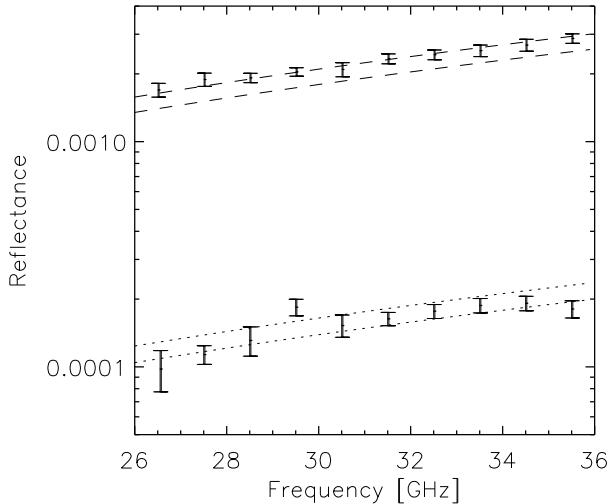


FIG. 11.— Comparison between laboratory reflectivity measurements and theory on 0.003 inch polypropylene situated at  $\theta = 45^\circ$ . Errors in the data are mostly systematic, arising from standing waves in the system. The uncertainty in the model is due to both thickness variations and uncertainties in the index of refraction of the dielectric sheet.  $R_{TE}$  corresponds to the upper set of curves (dashed), and  $R_{TM}$  to the lower set of curves (dotted).

while for the correlators

$$\text{NET}^{\text{corr}} = \kappa \frac{\sqrt{(T_{rec}^E + T_{load})(T_{rec}^H + T_{load})}}{\sqrt{\Delta\nu}},$$

where  $\kappa = \sqrt{2}$ , and  $\Delta\nu$  is the RF bandwidth. The most naive technique to obtain the NETs is simply to calculate the RMS of the time stream in a one-second segment and convert from voltage to temperature. This approach, however, over-estimates the NET, and only applies when the noise is white. In practice, the power spectrum exhibits an excess of low frequency power ( $1/f$  noise). These low-frequency components in the time-stream will dominate the RMS if they are not removed. A general expression for the post-detection spectral density of correlation and total power radiometers which includes the effects of gain fluctuations,  $\Delta G(f)$ , a system offset,  $T_{offset}$ , and offset fluctuations,  $\Delta T_{offset}(f)$ , is given by (Wollack 1995; Carretti et al. 2001):

$$P^{\text{corr}}(f) = 2 \frac{k^2 T_{sys}^2}{\Delta\nu} + T_{offset}^2 \Delta G^2(f) + \Delta T_{offset}^2(f), \quad (19)$$

$$P^{\text{TP}}(f) = 2 \frac{T_{sys}^2}{\Delta\nu} + T_{sys}^2 \Delta G^2(f) + \Delta T_{sys}^2(f). \quad (20)$$

Note that the second and third terms of equations 19 and 20 do not depend on the RF bandwidth,  $\Delta\nu$ , and do not integrate down with time. The audio frequency,  $f$ , dependence of the gain fluctuations for the HEMT amplifiers is  $\Delta G(f) \propto f^{-1}$  (Wollack 1995). These equations, along with figure 12 (which shows the power spectra of all three in-phase correlator channels and both total power detectors during an observation run) illustrate the relative performance tradeoffs of the total power polarimeter versus the correlation polarimeter. POLAR uses both types of radiometer; however, the total power polarimeter channel

is used only as an atmospheric monitor. The instantaneous difference between the two total power channels (TP-E and TP-H) is proportional to the Stokes Q parameter in the OMT frame, and after  $45^\circ$  rotation would provide the U parameter. However, for a total power receiver the HEMT gain fluctuation noise  $\Delta G(f)$  in equation 20 multiplies the *system* temperature ( $T_{sys} = T_{rec} + T_{ant}$ ) rather than the *offset* temperature as in equation 19. This produces the dramatic  $1/f$  rise in the total power detectors' PSD, which is greatly diminished for the correlator channels. This allows us to slowly modulate the signal by rotation of the radiometer at 33 mHz, rather than at several Hz as would be required for the total power channels. It is clear from the spectra that the correlators are far more sensitive and stable than the total power detectors.

The correlation radiometer offset is produced by signal power which is correlated between the two polarization states. This effect is primarily the result of imperfect cross polarization and polarization isolation of the OMT. The total spurious polarization generated by the OMT is due to both cross polarization and imperfect isolation. In figure 13 the isolation, cross polarization, insertion loss, and return loss are shown.

Since the correlation polarimeter offset is produced mainly by spurious polarization of the OMT, the dominant source of offset fluctuations will be from fluctuations in the antenna temperature of observed sources, primarily (unpolarized) atmospheric emission:  $T_{offset}(f) = \text{SP}_{omt} T_{atm}(f)$ , where  $\text{SP}_{omt}$  is the OMT's spurious polarization (sum of the isolation and cross-polarization). The OMT's cross-polarization dominates the spurious polarization, since the isolation between the polarization states is enhanced by

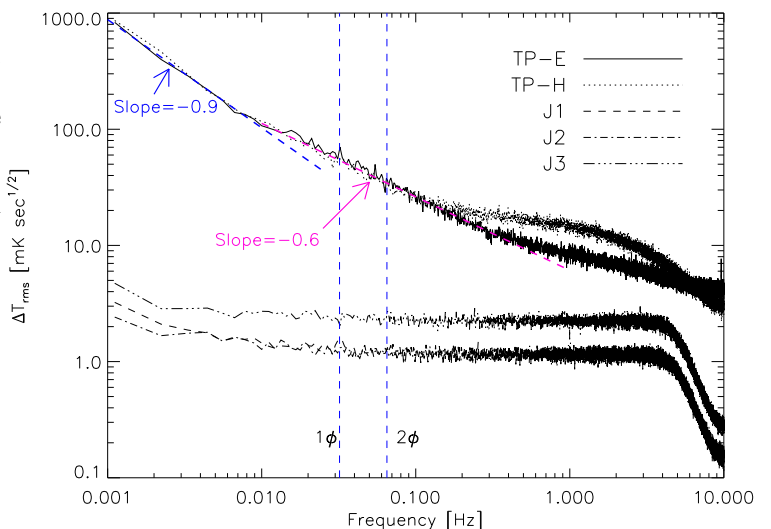


FIG. 12.— Power spectra of all five POLAR signal channels. The  $1/f$  behavior of the total power detectors, and the 5 Hz low-pass filtering of the anti-aliasing are evident. The CTI coldhead expansion/compression cycle is at 1.2 Hz, and no contamination is observed in the signal channels. Vertical lines indicate the rotation frequency ( $1\phi$ ) and the Stokes parameter modulation frequency ( $2\phi$ ). The low frequency rise in the total power detector spectra is due to both HEMT gain fluctuations (for  $f > 0.01$  Hz) and atmospheric fluctuations (for  $f < 0.01$  Hz). The low frequency rise in the correlator spectra at  $f < 0.01$  Hz is also indicative of atmospheric fluctuations.

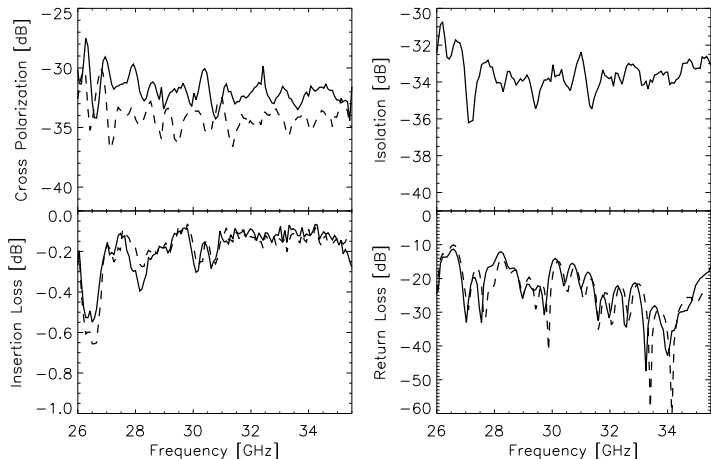


FIG. 13.— Properties of POLAR’s OMT. Isolation, cross-polarization, return loss, and insertion loss are shown across the  $K_a$  band. All properties improve at the highest RF frequencies, leading to decreased spurious polarization for channels J1 and J2 relative to J3.

cryogenic isolators. The atmospheric component of antenna temperature fluctuations at 30 GHz follows a Kolmogorov spectrum which falls as  $T_{atm}(f) \propto f^{-8/3}$  (Carretti et al. 2001). If the experiment is not modulated at a frequency much higher than the knee frequency of the fluctuation spectrum, these terms will dominate the system NET. This, of course, is the motivation for the modulation of the signal by rotation of POLAR. Throughout the Spring 2000 observing campaign POLAR was rotated at 0.033 Hz.

The stability of the offsets over a single rotation of the instrument is crucial to the recovery of the Stokes parameters. Note that the behavior of the noise should be independent of the phase of the reference waveform supplied to the lock-in. The QPC are insensitive to correlated signals, including uncorrelated atmospheric emission which is spuriously correlated by the OMT. The QPC therefore show almost no  $1/f$  noise, and provide powerful monitors of the intrinsic noise of the radiometer. Over the course of the 2000 observing campaign, we found periods of high offset and large offset fluctuations to be correlated with environmental effects, especially the occasional formation of dew and ice on the vacuum window.

### 5.2. Optical Cross Polarization

The corrugated scalar feed horn demonstrates low cross-polarization (Clarricoats & Olver 1984). However, even for an ideal and completely symmetric feed there is always non-zero cross-polarization. For an ideal horn, the cross-polarization induced by scattering in a plane containing the polarization axis is identically zero since there has been no polarization conversion. This is also manifestly true for scattering in a plane perpendicular to the polarization axis. However, using a simple geometric optics approximation it can be demonstrated (Clarricoats & Olver 1984) that there is polarization conversion (cross-polarization) which varies as  $\sin^2 \phi$ , and will be peaked at  $\phi = 45^\circ, 135^\circ, 225^\circ, 315^\circ$  where  $\phi$  is the azimuthal angle

in the aperture plane. The maximum cross-polarization of the feed was measured to be  $\leq -40$  dB (see figure 5). Again, the cross-polarization vanishes on axis, and it is primarily the off-axis response in the near side-lobes that show cross-polarization. As shown in Carretti et al. (2001), the quadrupolar anisotropy on scales comparable to the FWHM is the dominant source of spuriously correlated response by the feed. POLAR’s vertical drift scan geometry and low side-lobe level reduced the effect of cross-polarized optical response to negligible levels.

### 5.3. Non-Ideal Correlation Radiometer Behavior

The most common non-ideal behavior of the correlation radiometer results from electrical path length mismatch between the input arms. From equation (5) the correlator’s DC output is proportional to  $\cos(\Delta\phi_\nu)$  where  $\Delta\phi_\nu$  is the phase shift between the two arms of the radiometer. A  $90^\circ$  phase shift therefore results in a zero signal-to-noise ratio. If the phase difference is frequency dependent, as in the case of a path length mismatch, then the DC output of the correlator will be reduced by the cosine term. The path length difference  $\Delta L$  introduces a dispersive phase shift:  $\Delta\phi(\nu, \Delta L) = 2\pi\Delta L/\lambda = 2\pi\frac{\Delta L\nu}{c}$ . Assuming constant power spectra across the RF band for the source, beam, and radiometer transfer functions, from equation (5), we have:

$$R(0) \propto \int_{-\pi}^{+\pi} \tilde{\gamma}(\theta)\tilde{B}(\theta)|\tilde{H}|^2 d\theta \int_{\nu_o}^{\nu_o+\Delta\nu_{RF}} \cos\left(2\pi\frac{\Delta L\nu}{c}\right) d\nu. \quad (21)$$

The contribution of each spectral component is thus weighted by the cosine of its phase. Equivalently, the bandpass of the correlator is modulated by the cosine term. It is therefore imperative to accurately match the path lengths in the system. To determine the phase mis-match a completely polarized signal is injected into the OMT input. The injected signal is swept in frequency across the RF band. By measuring the frequency modulation of the correlator spectrum by the  $\cos \Delta\phi$  envelope, the equivalent electrical path length imbalance can be determined. The electrical path difference measurements agreed with measurements of the physical waveguide path difference. To balance the path lengths, sections of waveguide were added to the shorter arm of the receiver. The remaining non-ideality results from gain asymmetry between arms, across the band passes. These effects can be caused by mismatched bands, temperature dependence, and phase

TABLE 2  
TOLERANCES ON CORRELATION POLARIMETER FREQUENCY RESPONSE VARIATIONS FOR A 2.5% REDUCTION IN SIGNAL TO NOISE RATIO (RELATIVE BETWEEN ARMS).

Type of Variation	Permissible Level
Gain Slope	3.5 dB across band
Gain Sinusoidal Ripple	2.9 dB peak-peak
Polarization Band Centroid Offset	5% of $\Delta\nu_{RF}$
Phase Shift Between Bands	12.8°

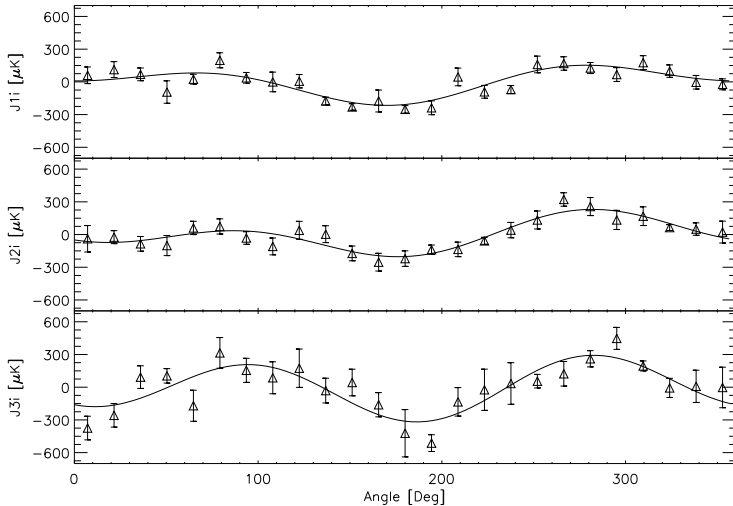


FIG. 14.— Correlator outputs binned into rotation angle for 206 rotations (1 hour 43 minutes) of data obtained during observations on 2 May 2000. Unpolarized offsets and Stokes parameter offsets are visible for each of the three correlator channels. The relative phasing and offset magnitudes are consistent with the model presented in section 5.4. Fits to the Stokes parameter offsets are presented in table 3.

instability of the amplifiers and/or the correlator. In practice it is impossible to eliminate all such effects, and so in table 2 we provide an estimate of the tolerable level of a few of these effects such that they would contribute to a 2.5% degradation of the signal-to-noise ratio of the correlation receiver (Thompson et al. 1998).

#### 5.4. Polarimetric Offsets

In the analysis, for each rotation of the polarimeter, the correlator outputs are binned into rotation angle  $\theta_t$  and fit to

$$I(\theta_t) = I_o + C \cos \theta_t + S \sin \theta_t + Q \cos 2\theta_t + U \sin 2\theta_t.$$

Figure 14 shows the output of 206 co-added rotations (1 hour 43 minutes of data) from the night of 2 May 2000 binned into a single rotation to increase the signal to noise ratio of the systematic effect. Fits to  $I_o, C, S, Q, U$  for these plots result in the Stokes parameter offsets for each channel in the instrumental coordinate system. The modulated signals are consistent with a common optical offset for each channel (as indicated by the consistent phasing of the signals across the channels). Unpolarized flux is correlated in the receiver due to the OMT’s cross polarization and imperfect isolation, causing  $I_o \neq 0$ . The offset is believed to be unpolarized, but anisotropic, with a dipolar and quadrupolar dependence on the rotation angle  $\theta_t$ , producing spuriously polarized components  $Q$  and  $U$ . The quadrupole anisotropy is most likely caused by the outer, reflecting, ground screen, which is a square ‘scoop’ centered on the dewar axis, while the dipole anisotropy is attributed to the feed horn being located  $\simeq 3$  inches radially outward from the dewar axis centerline. The dipolar ( $S$  and  $C$ ) and quadrupolar ( $Q$  and  $U$ ) components are present at levels that are 30 dB lower than the unpolarized offset  $I_o$ . The frequency dependence of the offset is

consistent with the OMT’s performance. Both the cross-polarization and the isolation of the OMT degrade with decreasing RF frequency. Therefore, since the radiometer offset is primarily due to the OMT’s cross-polarization, the offset will be largest for J3 since it is the lowest frequency band. Table 3 presents the offsets as a function of channel for a representative night of data. The offset phase dependence is roughly constant throughout the season, whereas the magnitude of the offsets are correlated between channels and vary with observing conditions; most notably humidity and atmospheric opacity.

The magnitude and phase of the offset are stable over  $\sim 4$  hour timescales. Our sensitivity to Stokes parameter offsets is minimized by constraining the demodulated data to have no dependence on an overall Stokes parameter offset. This is a generalization of the procedure outlined in Bond, Jaffe, & Knox (1998) to treat (unpolarized) offsets for CMB temperature anisotropy experiments. The offset removal procedure not only constrains the final maps produced to have zero offset, but also accounts for the sensitivity degradation induced by the offset removal. The offsets are computed from maps produced for each channel, for each section of data that survives the data editing criteria, by enforcing consistency where two sections measure the same pixel on the sky. This induces correlations between sections of data, and between adjacent pixels mapped in the same section. The results presented in Keating et al. (2001) are the most stringent presented to date at large angular scales.

## 6. METEOROLOGICAL EFFECTS AND DATA SELECTION

A variety of weather-related phenomena were encountered during the Spring 2000 observing campaign. We compiled data on the Pine Bluff, Wisconsin area from both the National Weather Service and the GOES-8 satellite data served by the Space Sciences and Engineering Center at the University of Wisconsin-Madison<sup>26</sup>.

### 6.1. General Atmospheric Effects

The GOES-8 data is recorded hourly, and measures a  $\simeq 5$  km by 5 km area, within 20 km of the POLAR observatory. It provided the cloud cover fraction of the area, and precipitable water vapor (PWV) column height (as well as a host of other weather variables). Historically, PWV in the area shows a strong seasonal dependence. Periods of high PWV correlated with formation of dew and ice on the vacuum window. Astrophysical data acquired during these periods were not used in the analysis due to the spurious correlation produced by reflection from the dew/ice on the window. Cloud cover fraction exhibits a bimodal histogram, with more than 35% of the time showing totally clear weather and about 15% of the time categorized as completely overcast. Partially cloudy days account for the other 50% of the distribution. POLAR’s two total power channels monitor the atmospheric zenith temperature in real time. Figure 15 presents a histogram of daily atmospheric zenith temperature measured over the observing season by POLAR.

<sup>26</sup> <http://www.ssec.wisc.edu>

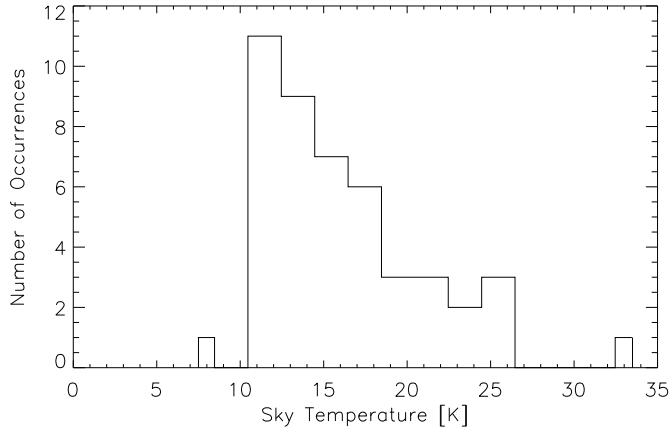


FIG. 15.— Daily atmospheric zenith antenna temperature distribution for the Spring 2000 observing campaign.

### 6.2. Solar and Lunar Effects

Based on the geometry of the inner, co-rotating, conical groundscreen, some solar radiation will enter this screen when sunlight propagates over the outer (fixed) groundscreen. This happens at a solar elevation of  $\simeq 10^\circ$ . However, for this light to enter the horn, it must scatter many times off the inner ground screen and will then be absorbed by the inner screen's Eccosorb coating. Below this elevation of  $10^\circ$ , solar radiation must undergo a double diffraction to enter the system. The amount of sunlight in the beam-pattern steeply increases as the sun rises until the sun's elevation reaches  $\simeq 49^\circ$ , at which time radiation from the sun can directly enter the horn. We found that, in practice, solar contamination was undetectable below a solar elevation of  $30^\circ$ . To be conservative, we eliminated all data taken with the sun more than  $20^\circ$  above the horizon. Since data were collected 24 hours per day, this represents a sizeable 38.6% of our data, or  $\simeq 288$  hours.

The moon is a bright microwave source, corresponding roughly to an thermodynamic temperature of 220 K. Its emission is dependent upon frequency, lunar phase, and polarization. Using the lunar emission model presented in Keihm (1983), the *COBE* team calculate the lunar emission in both polarization states at the 30, 50, 90 GHz, and show that the polarized lunar antenna temperature at 31 GHz is  $\lesssim 1K$  (Bennett et al. 1992). Using a variation of this model, and the POLAR beam patterns, we have estimated the polarized antenna temperature of the moon as a function of elevation angle. During the Spring 2000 observing season the highest lunar elevation was  $68.4^\circ$ . We removed all data when the moon was more than  $50^\circ$  in elevation; this corresponds to about 1.2% of the data, and reduces the lunar effect to be  $< 5 \mu K$ .

### 6.3. Atmospheric Data Cut

The primary data quality cut for selecting astrophysical data is based on the statistics of the  $S$  and  $C$  terms of fits to equation 7. This cut is referred to as the  $1\phi$  cut. As previously mentioned, the  $S$  and  $C$  components are statistically independent from the  $Q$  and  $U$  components. Since the  $1\phi$  component probes the power spectrum of the radiometer at lower frequencies, it is more susceptible to contamination by atmospheric fluctuations, and can there-

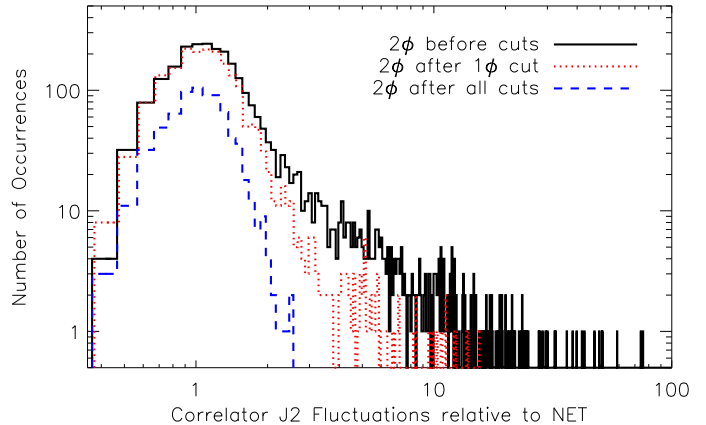


FIG. 16.— Distribution of correlator fluctuations for 7.5 minute averages, as a function of cut level. The solid curve shows the fluctuation level at twice the rotation frequency, relative to the NET of the system, for the in-phase channel J2I, after cuts removing sun, moon, and dew contamination have been applied. The dotted curve shows the same information, but after the  $1\phi$  cut has been applied. The dashed curve shows the distribution after all cuts have been applied; very little if any  $2\phi$  contamination remains.

fore be used as an unbiased probe of data quality which is independent of the astrophysical data. For each 7.5 minute segment of data, the fluctuations in  $S$  and  $C$  are compared to 1) the expected fluctuation level from gaussian white noise and 2) fluctuations in  $S$  and  $C$  from the QPC which, as mentioned, display pure white noise power spectral densities with amplitude equal to the radiometer NET. Figure 16 shows the distribution of fluctuations in the  $2\phi$  component for the 7.5 minute averages for channel J2, for the Spring 2000 observing campaign. Also indicated are the cut levels used in the analysis presented in Keating et al. (2001) and the IPC distribution after the  $1\phi$  cut has been applied.

## 7. SUMMARY

We have described the design and performance of a novel instrument which was recently used to set upper limits on the polarization of the CMB. The simplicity of the optical design of the polarimeter and the observing strategy resulted in minimal systematic effects. Observations were conducted from a convenient location near the University of Wisconsin – Madison. The site was useful for work at 30 GHz and its proximity afforded us the ability to diagnose problems and make rapid adjustments to optimize instrumental performance while still in the field. While no evidence for CMB polarization was detected with POLAR, the precision of the upper limits are impressive given the brief observing season available during Spring 2000. This is attributable to the low noise of the HEMT amplifier front-end and the modest modulation requirements permitted by the correlation radiometer back-end. POLAR has proven to be extremely versatile and stable. Starting in January 2001 the POLAR radiometer has been used as the receiver in a search for CMB polarization at small angular scales: COsmic Microwave Polarization at Small Scales (COMPASS). Results from COMPASS are forthcoming and will further demonstrate the viability of the correlation polarimeter technique.

TABLE 3  
 POLAR OFFSETS 2 MAY 2000. 206 ROTATIONS (1 HOUR 43 MINUTES OF DATA) CO-ADDED  
 AND BINNED INTO ROTATION ANGLE <sup>†</sup>

Channel <sup>a</sup>	$I_o^b$ [mK]	$C^c$ [ $\mu$ K]	$S^d$ [ $\mu$ K]	$Q^e$ [ $\mu$ K]	$U^f$ [ $\mu$ K]
J3I	$133.8 \pm 1.0$	$75.7 \pm 38.0$	$-31.7 \pm 38.0$	$-23.6 \pm 38.0$	$-73.6 \pm 38.0$
J2I	$83.6 \pm 1.0$	$76.2 \pm 20.0$	$-91.3 \pm 20.0$	$-125.8 \pm 20.0$	$-25.9 \pm 20.0$
J1I	$88.1 \pm 1.0$	$108.3 \pm 20.0$	$-48.4 \pm 20.0$	$-99.3 \pm 20.0$	$21.0 \pm 20.0$
J3Q	$15.76 \pm 0.09$	$13.8 \pm 20.0$	$15.0 \pm 20.0$	$8.4 \pm 20.0$	$68.9 \pm 20.0$
J2Q	$5.57 \pm 0.05$	$-9.6 \pm 20.0$	$-25.3 \pm 20.0$	$29.6 \pm 20.0$	$-28.0 \pm 20.0$
J1Q	$7.15 \pm 0.04$	$7.3 \pm 20.0$	$-19.1 \pm 20.0$	$-20.3 \pm 20.0$	$12.7 \pm 20.0$

<sup>†</sup> refer to Fig. 14 for data.

<sup>a</sup> ‘I’ refers to in-phase channels; ‘Q’ refers to quad-phase channels.

<sup>b</sup> Unpolarized, unmodulated, intensity.

<sup>c</sup> Dipole modulated cosine term.

<sup>d</sup> Dipole modulated sine term.

<sup>e</sup> Quadrupole modulated  $Q$  term.

<sup>f</sup> Quadrupole modulated  $U$  term.

We are grateful to a number of people who influenced the design and analysis of POLAR. Initial theoretical guidance and encouragement came from Alex Polnarev and Robert Brandenberger. Dick Bond, Robert Crittenden, Angelica de Oliveira-Costa, Wayne Hu, Lloyd Knox, Arthur Kosowsky, Kin-Wang Ng, and Matias Zaldarriaga provided crucial insight during the development and analysis phases, and vastly enhanced the scientific impact of the project. We are also indebted to several experimentalists who worked-on, supported, or guided, the construction of the instrument: Brendan Crill, Khurram Farooqui, Kip Hyatt, Slade Klawikowski, Alan Levy, Phil Lubin, Melvin Phua, Dan Swetz, David Wilkinson, Grant Wilson, Ed Wollack. BGK and CWO were supported by NASA GSRP Fellowships. POLAR's HEMT amplifiers were provided by John Carlstrom. This work has been supported by NSF grants AST 93-18727, AST 98-02851, and AST 00-71213, and NASA grant NAG5-9194.

## REFERENCES

- Bennett, C. L., et al. 1992, ApJ, 391, 466  
 Bond, J. R., Jaffe, A. H., & Knox, L. 1998, Phys. Rev. D57, 2117  
 Brouw, W. N., & Spoelstra, T.A. 1976, A&AS, 26, 129  
 Carretti, E., et al. 2001, New Astronomy, 6, 173  
 Chandrasekhar, S. 1960, *Radiative Transfer*, Dover, New York  
 Cheng, E., et al. 1979, ApJ, 232, L139  
 Chu, T. 1975, Bell Sys. Tech. J., 54, 1665  
 Clarricoats, P. & Olver, A., 1984 *Corrugated horns for microwave antennas*, Peter Peregrinus  
 Davies, R. D., et al. 1996, MNRAS, 278, 883.  
 Draine, B. T. & Lazarian, A. 1998, ApJ, 494, L19  
 Faris, J., 1966, J. of Results of the NBS, 71C  
 Fujimoto, K., 1964, IEEE-MTT, March p. 203  
 Gasiewski, A., & Kunkee, D. 1993, IEEE-MTT, 41, 767  
 Gunn, J. E. & Peterson, B. A. 1965, ApJ, 142, 1633  
 Hu, W., and White, M. 1997, New Astron., 2, 323  
 Janssen, M.A., et al. 1979, IEEE Trans. Antennas and Prop. 27(4), 551  
 Johnson, D., & Wilkinson, D. 1987, ApJ, 313, L1  
 Jackson, J. D., 1975, *Classical Electrodynamics*, Wiley  
 Kamionkowski, M., Kosowsky, A., and Stebbins, A. 1997, Phys. Rev. D, 55, 7368  
 Keating, B., Polnarev, A., Steinberger, J., & Timbie, P. 1998, ApJ, 495, 580  
 Keating, B., et al., 2001, ApJ, 560, L1  
 Keihm, S.J. 1983, Planetary Sci. Inst. Rep., K.  
 Kraus, J. 1986 *Radio Astronomy*, McGraw-Hill, New York  
 Lubin, P., & Smoot, G. 1981, ApJ, 245, 1 L51  
 Mason, B., et al. 1999, AJ, 118, 2908  
 Nanos, G. 1979, ApJ, 232, 341  
 Netterfield, C.B., et al., 1995, ApJ, 474, L69  
 O'Dell, C.W., et al. 2002, IEEE MTT, accepted  
 Pospieszalski, M. 1992, IEEE MTT-S Digest, 1369  
 Pozar, D. 1990, *Microwave Engineering*, New York, Addison-Wesley  
 Rohlfs, K. 1996, *Tools of Radio Astronomy*,  
 Rybicki, G. B., & Lightman, A. 1979, *Radiative Processes in Astrophysics*, New York, Wiley)  
 Sironi, G. et al. 1997, New Astron., 3, 1  
 Tegmark, M. 1997, Phys. Rev. D, 56, 4514  
 Tegmark, M., & de Oliveira-Costa, A. 2001, Phys. Rev. D, 64, 63001  
 Thompson et al., 1998, *Interferometry and synthesis in radio astronomy*, Krieger, Malabar  
 Timbie, P., & Wilkinson, D. 1990, ApJ, 353, 140  
 Wang, X., Tegmark, M. & Zaldarriaga, M. 2001, astro-ph/0105091  
 Wollack, E.J. 1995, Rev. Sci. Inst. 66, 4305  
 Wollack, E.J., and Pospieszalski, M., 1998, IEEE MTT-S Digest, 669  
 Wollack, E.J., et al., 1997, ApJ, 476, 440  
 Zaldarriaga, M., & Seljak, U. 1997, Phys. Rev. D, 55, 1830  
 Zaldarriaga, M., Spergel, D., Seljak, U. 1997 ApJ, 488, 1  
 Zaldarriaga, M. 1997, Phys. Rev. D, 55, 1822  
 Zaldarriaga, M. 1998, ApJ, 503, 1  
 Zhang, X., et al. 1993, IEEE-MTT 41, 8